

A thesis submitted in fulfilment of the requirements
for a Master's degree in Physics

Physics-informed deep-learning for low-field MRI reconstruction and denoising

by
Leonid Lunin
born at 16.01.1999
Matriculation number: 402920

Berlin, 21.01.2026

First examiner: Prof. Dr. Ralph Ernstorfer
Second examiner: Dr. Christoph Kolbitsch
Supervisor: David Schote

Eidesstattliche Erklärung

1. Hiermit versichere ich, dass ich die vorliegende Arbeit ohne Hilfe Dritter und ausschließlich unter Verwendung der aufgeführten Quellen und Hilfsmittel angefertigt habe. Alle Stellen, die den benutzten Quellen und Hilfsmitteln unverändert oder inhaltlich entnommen sind, habe ich als solche kenntlich gemacht.
2. Sofern generative KI-Tools verwendet wurden, habe ich Produktnamen, Hersteller, die jeweils verwendete Softwareversion und die jeweiligen Einsatzzwecke (z.B. sprachliche Überprüfung und Verbesserung der Texte, systematische Recherche) benannt. Ich verantworte die Auswahl, die Übernahme und sämtliche Ergebnisse des von mir verwendeten KI-generierten Outputs vollumfänglich selbst.
3. Die Satzung zur Sicherung guter wissenschaftlicher Praxis an der TU Berlin vom 8. März 2017* habe ich zur Kenntnis genommen.
4. Ich erkläre weiterhin, dass ich die Arbeit in gleicher oder ähnlicher Form noch keiner anderen Prüfungsbehörde vorgelegt habe.

Berlin, 21.01.2026
Ort, Datum

Leonid Lunin,
Vollständiger Name, Unterschrift

*https://www.static.tu.berlin/fileadmin/www/10000060/FSC/Promotion___Habilitation/Dokumente/Grundsaezze_gute_wissenschaftliche_Praxis_2017.pdf

Abstract

Magnetic Resonance Imaging (MRI) technique is a powerful diagnostic tool for medical diagnostics. Conventional High-Field (HF) MRI systems of 1.5 to 3 T offer high-resolution images with low noise. Nonetheless, HF MRI systems are expensive, immobile, require complex infrastructure and have high maintenance expenses, what makes MRI diagnostic inaccessible for most of the world population. Recent developments in Ultra-Low-Field (ULF) MRI of less than 100 mT offer a complementary cost-effective and portable solution for rapid screening and applications in emergency conditions. However, ULF MRI systems provide significantly lowered Signal-to-Noise Ratio (SNR) compared to conventional HF MRI systems.

Technical limitations of ULF MRI systems pose a challenge for the MRI reconstruction process to provide an image quality suitable for diagnostic interpretation. Conventional reconstruction techniques, suitable for HF MRI systems, do not always yield high-quality results for the ULF MRI data. In the past decades, deep-learning based techniques became a widely used tool for data processing tasks, including MRI reconstruction problem.

In this thesis, I present a novel approach of a complex-valued deep-learning model for ULF MRI reconstruction, particularly for increase of resolution (*super-resolution*) and noise reduction (*denoising*) problems. Different training schemes were examined to determine the model configuration that achieved the best performance across image quality metrics. In parallel to the experiments related to the complex-valued deep-learning model, a magnitude-only deep-learning model with an analogous architecture was developed and employed as a reference for the complex-valued deep-learning model.

Both of the complex-valued and magnitude-only deep-learning models demonstrated high and very similar results of image quality metrics for super-resolution and denoising problems, yielding an increase of median Structural Similarity Index Measure (SSIM) from approx. 69 % up to approx. 90 %, median Peak Signal-to-Noise Ratio (PSNR) from 29 dB up to 33 dB, and reducing median Mean-Square-Error (MSE) by factor of approx. 2.6 in comparison with the reconstruction by inverse Fourier transform of raw data padded with zeros in k -space.

Furthermore, the developed complex-valued deep-learning model served as a foundation for the physics-informed deep-learning model that combines the deep-learning approach with the underlying physical model of ULF MRI acquisition process. Then, these models were challenged for both fully sampled and accelerated measurements, yielding comparable results for the SSIM, PSNR and MSE image quality metrics, with small performance gap of the magnitude-only deep-learning model of less than 1.5 %.

Finally, the prepared reconstruction models, previously evaluated on the synthetic dataset, were applied to the *in vivo* measurement acquired with a real-world ULF MRI scanner of 50 mT. The complex-valued deep-learning model and the physics-informed model demonstrated an ability of better noise suppression for fully sampled measurement, compared to the magnitude-only deep-learning model.

Zusammenfassung

Die Technik der Magnetresonanztomographie (MRT) entwickelte sich heutzutage zu einem leistungsvollen Instrument der medizinischen Diagnose. Herkömmliche Hoch-Feld (HF) MRT Systeme mit einer Magnetfeldstärke in Höhe von 1,5 to 3 T sind in der Lage, die hochauflösten Aufnahmen mit geringem Rauschen aufzunehmen. Allerdings sind die HF MRT Systeme teuer, stationär, erfordern eine komplexe Infrastruktur und auferlegen die hohen Betriebs- und Wartungskosten. Infolgedessen bleibt das MRT Verfahren für den größten Teil der Weltbevölkerung unzugänglich.

Neue Entwicklungen im Bereich von Ultra Nieder Feld (ULF) MRI mit weniger als 100 mT bieten eine komplementäre, kostenreduzierte und mobile Lösung für rapide Untersuchungen und Anwendungen bei Notfällen. Die ULF MRI Systeme liefern jedoch ein deutlich geringeres Signal zu Rausch Verhältnis (SNR) im Vergleich zu herkömmlichen HF MRI Systemen.

Technische Limitierungen von ULF MRI Systemen erschweren die direkten Erzeugung von aussagekräftigen Aufnahmen. Übliche Rekonstruktionsverfahren, die für HF MRI Systeme geeignet sind, sind nicht immer gut anwendbar für die mit ULF MRI erzeugten Daten. In den letzten Jahrzehnten fanden die Deep Learning (DL) basierten Verfahren eine breite Anwendung in der Daten Verarbeitung, auch für das MRT Rekonstruktion Problem.

In dieser Arbeit wurde der neuartige Ansatz eines komplexwertigen DL Modells für ULF MRI Rekonstruktion präsentiert, insbesondere für die partikulären Probleme von der Auflösungserhöhung (*Super-Resolution*) und für Rauschunterdrückung (*Denoising*). Mehrere Konfigurationen von DL Modellen wurden getestet, um diejenige Konfiguration zu finden, welche die besten Ergebnisse für die Bildqualitätsmetriken liefert. Das komplexwertige DL Modell wurde mit einem Referenzmodell vergleichbarer Architektur, das nur die Betragswerte berücksichtigt, verglichen.

Die beiden DL Modelle demonstrierten hohe und sehr ähnliche Rekonstruktionsqualität bei Super-Resolution und Denoising Problemen. Nämlich wurde der Median von Structural Similarity Index Measure (SSIM) Metrik von etwa 69 % auf etwa 90 % erhöht, sowie der Median von Peak Signal to Noise Ratio (PSNR) von 29 dB auf 33 dB, und Reduktion des Medians von Mean Square Error (MSE) um etwa den Faktor 2,6 im Vergleich mit den Rohdaten, die durch die Auffüllung mit Nullen im k -Raum und inverse Fourier-Transformation rekonstruiert wurden.

Weiterhin diente das entwickelte komplexwertige DL Modell als Grundlage für ein physik-informiertes DL Modell, das den DL Ansatz mit dem zugrunde liegenden physikalischen Modell des ULF MRI Aufnahmeprozesses kombiniert. Diese Modelle wurden sowohl für Daten mit sowohl vollständig, als auch partiell abgetasteten Daten getestet. Beide Modelle lieferten vergleichbare Ergebnisse für SSIM, PSNR und MSE Qualitätsmetriken, mit einem kleinen Leistungsvorsprung des Betragswert-basierten DL Modells von etwa 1,5 %.

Zuletzt wurden die entwickelten Modelle, die zuvor mit einem synthetischen Datensatz getestet wurden, auf eine *in vivo* Messung mit einem realen ULF MRI Scanner mit 50 mT angewendet. Die komplexwertigen und physik-informierten DL Modelle demonstrierten eine bessere Rauschunterdrückung für die *in vivo* Aufnahmen im Vergleich zu Vorhersagen des Betragswert-basierten DL Modells.

Contents

1	Introduction	1
2	Theory	4
2.1	Acquisition principle of MRI	4
2.1.1	Microscopic spin dynamics in static magnetic field	4
2.1.2	Macroscopic spin dynamics and relaxation concepts	5
2.1.3	Spatially resolved acquisition principle	7
2.1.4	Single- and multi-coil acquisitions	9
2.2	General reconstruction problem	9
2.3	Deep-Learning model	11
2.3.1	Artificial neural network	11
2.3.2	Convolutional neural networks	13
2.3.3	Complex valued network approach	13
2.4	Challenges of low-field MRI system	14
3	Image-base super-resolution and denoising	16
3.1	Introduction	16
3.2	Methods	17
3.2.1	Deep-Learning models implementation	17
3.2.2	Training dataset preparation	17
3.2.3	Super-resolution and denoising problem	18
3.3	Experiments	19
3.3.1	Super-resolution and denoising problem	19
3.4	Results	20
3.4.1	Training dataset preparation	20
3.4.2	Super-resolution and denoising problem	21
3.5	Discussion	24
4	Physics-informed reconstruction model	26
4.1	Introduction	26
4.2	Methods	27
4.2.1	Regularisation problem for the acquisition model operator	27
4.2.2	End-to-end training	28
4.3	Experiments	29
4.3.1	Super-resolution and denoising problem	30
4.3.2	Super-resolution, denoising and undersampling problem	30
4.4	Results	31
4.4.1	Super-resolution and denoising problem	31
4.4.2	Super-resolution, denoising and undersampling problem	33
4.5	Discussion	39
4.5.1	Super-resolution and denoising problem	39
4.5.2	Super-resolution, denoising and undersampling problem	40

5 Application for <i>in vivo</i> data	42
5.1 Introduction	42
5.2 Methods	42
5.3 Experiments	43
5.4 Results	43
5.4.1 Brain T2 relaxation time contrast acquisition	43
5.4.2 Brain proton density contrast acquisition	47
5.5 Discussion	48
6 Conclusion and Outlook	50

Glossary

List of Abbreviations

ANN Artificial Neural Network

CA Channel Attention

CNN Convolutional Neural Network

CSM Coil Sensitivity Map

DFT Discrete Fourier Transform

DL Deep-Learning

E2E End-to-End

EMI Electromagnetic Interference

FFT Fast Fourier Transform

FOV Field Of View

GS Gaussian Sampling

GT Ground Truth

HF High-Field

LF Low-Field

LUMC Leiden University Medical Center

mRCAB Modified Residual Channel Attention Block

MRI Magnetic Resonance Imaging

MSE Mean-Squared Error

NMR Nuclear Magnetic Resonance

PD Proton-Density

PF Partial Fourier

PINN Physics-Informed Neural Network

PSNR Peak Signal-to-Noise Ratio

RCAN Residual Channel Attention Network

RF Radio Frequency

RG Residual Group

SNR Signal-to-Noise Ratio

SSIM Structural Similarity Index Measure

TSE Turbo Spin Echo

UHF Ultra-High-Field

ULF Ultra-Low-Field

1 Introduction

In the past decades Magnetic Resonance Imaging (MRI) became one of the most powerful and often used non-invasive tools for medical diagnostics and clinical research. In Germany alone, as of 2022, the annual number of examinations using MRI scanners exceeded 13 million and has shown steady growth through the past decade [1].

Unlike imaging techniques relying on the contrast caused by different transmission absorption depending on the tissue density (as medical X-rays or computer tomography techniques), MRI is based on Nuclear Magnetic Resonance (NMR) [2], where the temporal behaviour of collective magnetisation strength signal is measured after an excitation.

The characteristics of the emitted signal strongly depend on the local environment of each nucleus, such as the chemical compound it belongs to. By exploiting these differences with various measurement techniques, NMR can distinguish between different types of tissues.

In the 1970, Paul Lauterbur [3] and Peter Mansfield [4] conducted the first spatially resolved NMR measurements, providing the foundation for the development of MRI technique. This work was recognised with the Nobel Prize in Physiology or Medicine in 2003 [5]. Shortly after the pilot experiments, the first commercially available MRI scanners became available for clinical applications.

Since then, MRI systems have evolved in terms of hardware and software design, offering a well-established framework for routine diagnostic measurements, especially in brain diagnostics.

Despite their advantages, conventional MRI scanners are expensive, large-scale, stationary machines. They require complex infrastructure, including Radio Frequency (RF) shielded rooms, cryogenics for superconducting magnets and high-power power supply. The high costs of the machines and their expensive maintenance restrain the pace of widespread adoption of MRI scanners [6], resulting in access for only to approximately 10 % of the world's population [7]. In addition, the stationary nature of these systems often makes them inaccessible to critical patient groups, such as those in emergency or intensive care, where mobility and rapid diagnostic screening are essential.

These challenges and limitations of conventional MRI scanners raised interest in alternative, more accessible MRI scanners that maintain sufficient diagnostic capabilities while reducing hardware complexity and cost. Among these, the development of Low-Field (LF) (static magnetic field $< 550 \text{ mT}$) and Ultra-Low-Field (ULF) (static magnetic field $< 100 \text{ mT}$) MRI systems [8–12] is gaining traction in past decades.

Although LF scanners already offer substantially lowered purchase prices (up to 50 %), reduced associated installation expenses and maintenance costs (compared to a conventional 1.5 T scanner [13]), they still remain large stationary machines and unaffordable for many healthcare institutes.

The ULF systems are not intended to replace conventional and LF MRI scanners, but are designed to complement them by serving in rapid mobile screening applications and providing access for vast world's population for significantly reduced price [14].

Parallel to hardware developments, the research field of MRI data reconstruction also made progress, allowing to achieve a better reconstruction quality for the same set of acquired data, or

reduce measurement data but maintain the reconstruction quality. Various reconstruction techniques were proposed, driven by advances in computational methods and, more recently, by machine learning. Traditional reconstruction algorithms and numerical iterative techniques have been complemented and, in some cases, outperformed by machine learning-based approaches.

Artificial Neural Networks (ANNs) and Convolutional Neural Networks (CNNs), as a particular case of machine learning techniques, have demonstrated remarkable capabilities for image processing. Research in this field was recognised with the Nobel Prize in Physics in 2024 [15]. CNNs have proven effective for such tasks as reduction of the data noise level (denoising) [16] and increase of image resolution (super-resolution) [17] in many research fields. The MRI reconstruction problem is not an exception and the machine learning techniques for reconstruction problems are widely used in commercial MRI scanners and are approved for clinical use [18].

The novel concept of Physics-Informed Neural Networks (PINNs) [19], combining data-driven machine learning and prior physical model of a physical process to improve generalisability and stability of the model, was successfully used in MRI reconstruction problem [20, 21].

The advancements made by machine learning in MRI reconstruction problem are particularly relevant for ULF MRI, where traditional reconstruction techniques struggle with low Signal-to-Noise Ratio (SNR) of the measurement data. Machine learning embedded reconstruction algorithms were successfully demonstrated [22–26] and an image reconstruction technology using Deep-Learning (DL) received Food and Drug Administration (FDA) clearance in the US [27].

The potential of physics-informed DL reconstruction model for ULF MRI demonstrated promising results [28] in distortion correction and noise reduction problems. In the present thesis I introduce a novel physics-informed DL reconstruction model for noise reduction and resolution enhancement. In contrast to conventional models, leveraging only the magnitudes of MRI image, the proposed method uses complex-valued data, allowing native integration of the underlying physics acquisition model. In the present thesis I study and evaluate performance of the proposed novel model for the noise reduction and resolution enhancement problem for the full and reduced measurement data, compared with alternative state-of-the-art solutions.

In Chapter 2 a general overview of the basics of MRI working principle, data acquisition, reconstruction problem are given. In addition the general principles of application of DL models are introduced. In Chapter 3, establishment of the framework for experiments including the formation of the experimental dataset for ULF from the publicly available dataset of 3 T, development of the DL model and reconstruction performance evaluation is described. In Chapter 4 the previously developed DL reconstruction model is extended to physics-informed model and its performance is evaluated. Then, the performance of the developed models is compared depending on the quality of input data. In the final Chapter 5 application of the previously developed reconstruction models is evaluated for the data measurements acquired with the real-world ULF MRI scanner.

The software source code used for the experiments, as well as the \LaTeX source code of this document, are provided in the dedicated GitHub repository*.

The multimodal large language model GPT-5 developed by OpenAI was used to support writing and providing tips for stylistic formulation of certain text passages.

*<https://github.com/lrlunin/ptb-master-thesis-full>

2 Theory

In the first step, the theory of underlying physical concepts of Magnetic Resonance Imaging (MRI) will be discussed in a semi-classical picture, omitting the exact quantum mechanical description. This part is based on [29–31]. The reader can refer to [32] for a very brief overview of the concepts involved in the working principle of an MRI scanner.

Then, the mathematical problem of the MRI reconstruction as an inverse problem of acquisition will be formulated. Furthermore, introduction into a concept of Deep-Learning (DL) technique and its role in the inverse reconstruction problem is explained. And finally, the particular challenges of Ultra-Low-Field (ULF) MRI are discussed.

2.1 Acquisition principle of MRI

MRI technique exploits the fundamental effect of Nuclear Magnetic Resonance (NMR), interaction of a nuclei with electromagnetic radiation in an external magnetic field. In medical imaging, MRI primarily relies on hydrogen atoms because of their high prevalence in the human body. Spatially resolved imaging is performed by special sequences of temporary synchronized application of external magnetic field and of electromagnetic radiation pulses.

In the present Section, the time dynamics of isolated nucleus spin in the external magnetic field is derived. Afterwards, a macroscopic picture of dynamics of many spins is considered. Finally, main principles of spatially resolved imaging measurements are introduced.

2.1.1 Microscopic spin dynamics in static magnetic field

Magnetic moment of a nucleus with angular momentum \mathbf{J} and gyromagnetic ratio γ yields

$$\boldsymbol{\mu} = \gamma \mathbf{J} \quad (2.1)$$

Temporal dynamics of magnetic momentum $\boldsymbol{\mu}$ in static magnetic field \mathbf{B} is described by the following differential equation:

$$\frac{d\boldsymbol{\mu}}{dt} = \gamma \boldsymbol{\mu} \times \mathbf{B}, \quad (2.2)$$

In a three-dimensional space with a Cartesian coordinate system defined by set of unit vectors \mathbf{e}_x , \mathbf{e}_y and \mathbf{e}_z in the presence of uniform magnetic field along the z -axis $\mathbf{B} = B \mathbf{e}_z$, Equation 2.2 can be reformulated as a system of three scalar differential equations:

$$\begin{cases} \dot{\mu}_x(t) &= \gamma \mu_y(t) B \\ \dot{\mu}_y(t) &= -\gamma \mu_x(t) B \\ \dot{\mu}_z(t) &= 0 \end{cases} \quad (2.3)$$

The equation system yields a general case solution with substitution $\omega_0 = \gamma B$ (*Larmor frequency*) and given initial conditions for $\mu_x(t = 0)$, $\mu_y(t = 0)$ and $\mu_z(t = 0)$:

$$\begin{cases} \mu_x(t) &= \mu_x(0) \cos(\omega_0 t) + \mu_y(0) \sin(\omega_0 t) \\ \mu_y(t) &= \mu_y(0) \cos(\omega_0 t) + \mu_x(0) \sin(\omega_0 t) \\ \mu_z(t) &= \mu_z(0) \end{cases} \quad (2.4)$$

This represents an angular motion around the z -axis with a constant angular velocity ω_0 linearly proportional to the magnetic field amplitude B .

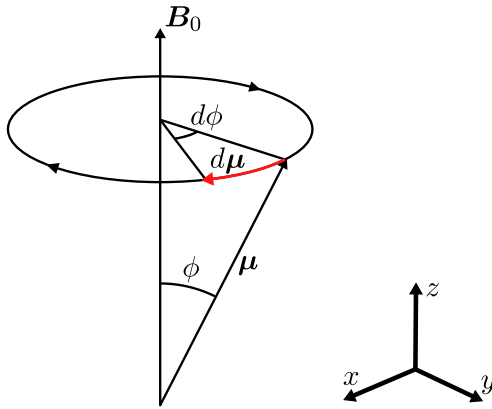


Figure 1: Precession of the magnetic moment μ in the external field B_0 .

2.1.2 Macroscopic spin dynamics and relaxation concepts

A very common concept for simplification of mathematical description in NMR and MRI is a rotating reference frame (*rotating frame*), where the precessing nucleus appears stationary. From now on the magnetisation dynamics is observed in rotating frame with angular velocity matching the Larmor frequency.

Assuming a large number of nuclei within volume V , the net magnetisation \mathbf{M} can be expressed as follows

$$\mathbf{M} = \frac{1}{V} \sum_i \mu_i \quad (2.5)$$

With assumption that all the nuclei have the same phase of motion and neglecting the mutual interaction, the collective magnetisation dynamics in presence of static magnetic field \mathbf{B}_0 can be derived by summing the equations of motion for an isolated nucleus, given in Equation 2.2:

$$\frac{1}{V} \sum_i \frac{d\mu_i}{dt} = \frac{\gamma}{V} \sum_i \mu_i \times \mathbf{B}_0 \quad (2.6)$$

or equivalently

$$\frac{d\mathbf{M}}{dt} = \gamma \mathbf{M} \times \mathbf{B}_0 \quad (2.7)$$

Net magnetisation \mathbf{M} can be decomposed into transversal \mathbf{M}_\perp and longitudinal \mathbf{M}_\parallel components

$$\begin{cases} \mathbf{M}_\perp &= M_x \mathbf{e}_x + M_y \mathbf{e}_y \\ \mathbf{M}_\parallel &= M_z \mathbf{e}_z \end{cases} \quad (2.8)$$

According to Equation 2.7 the time derivatives of transversal and longitudinal components yield

$$\begin{cases} \frac{d\mathbf{M}_\perp}{dt} &= \gamma \mathbf{M}_\perp \times \mathbf{B}_0 \\ \frac{d\mathbf{M}_\parallel}{dt} &= 0 \end{cases} \quad (2.9)$$

Potential energy U_M associated with net magnetisation \mathbf{M} in presence of magnetic field \mathbf{B}_0 is

$$U_M = -\mathbf{M} \cdot \mathbf{B}_0 = -M_z B_0 \quad (2.10)$$

and is dependent only on the longitudinal component M_z of net magnetisation. With good agreement of Curie's law for $\mu B/kT \ll 0$ at normal human body temperature of approx. 310 K, the equilibrium longitudinal magnetisation M_0 can be approximated as

$$M_0 = C \frac{B_0}{T}, \quad (2.11)$$

with C being a material-specific constant. In case of short-term perturbation of nuclei by Radio Frequency (RF) pulse, the equilibrium state is firstly disturbed with consequent recovery to its equilibrium state due to the energy dissipation to the environment. With a two-state model of the proton spins, the dynamics of the longitudinal component can be approximated as

$$\frac{dM_z}{dt} = \frac{1}{T_1} (M_0 - M_z) \quad (2.12)$$

with a T_1 being a tissue-specific experimental "spin-lattice relaxation time", yielding a solution for $M_z(t)$ with a given initial condition $M_z(0)$:

$$M_z(t) = M_z(0) e^{-t/T_1} + M_0 (1 - e^{-t/T_1}) \quad (2.13)$$

The dynamics of the transversal component of net magnetisation \mathbf{M}_\perp is dominantly characterised by the coherence of individual spin precessions. High degree of phase coherency of their individual transversal components sum up constructively and result a strong transversal net magnetisation. As the collective motion of individual spins dephases over time, the net transversal magnetisation decays.

With introduction of a characteristic "spin-spin relaxation time" T_2 , the differential equation for transversal net magnetisation component \mathbf{M}_\perp is given as

$$\frac{d\mathbf{M}_\perp}{dt} = \gamma \mathbf{M}_\perp \times \mathbf{B}_0 - \frac{1}{T_2} \mathbf{M}_\perp \quad (2.14)$$

and has the following solution with given initial condition $\mathbf{M}_\perp(0)$

$$\mathbf{M}_\perp(t) = \mathbf{M}_\perp(0) e^{-t/T_2} \quad (2.15)$$

Final differential equation for the dynamics of net magnetisation \mathbf{M} comes up from dynamics of longitudinal and transversal components, derived in Equations 2.12 and 2.14, and called *Bloch equation*:

$$\frac{d\mathbf{M}}{dt} = \gamma \mathbf{M} \times \mathbf{B}_0 + \frac{1}{T_1} (M_0 - M_z) \mathbf{e}_z - \frac{1}{T_2} \mathbf{M}_\perp \quad (2.16)$$

The T_1 and T_2 relaxation times vary across different tissues, being an origin of contrast in MRI. Special sequences of synchronised RF excitation pulses and magnetisation measurements can be employed for estimation of relaxation times. In the next subsection the concept of spatially resolved measurements of the relaxation times is introduced.

2.1.3 Spatially resolved acquisition principle

The key principle of spatially resolved acquisition in MRI is the controlled perturbation of the external magnetic field \mathbf{B}_0 in space, such that the measured magnetisation signal over the acquisition time allows to unambiguously assign the relaxation time to a dedicated area in three-dimensional space.

Typically, linearly increasing magnetic fields (*gradient fields*) along the x , y and z spatial axes are applied. The variation of an external magnetic field directly affects the resonance frequency of a proton spin which allows to encode a spin position through variation of its resonant frequency (*frequency encoding*). Gradient field can be applied in combination with a frequency-selective RF pulse in order to excite a specific slice only (*slice selection gradient*) or whilst the signal acquisition step (*readout gradient*). Other axis can be encoded via a temporal application of the linear gradient field which induces a phase shift along a specific axis (*phase encoding*).

A special temporally arranged series of alternating gradient fields along specific axes, variation of gradient field strength, application of RF excitation pulses, and measurements of magnetisation signal is called an *MRI sequence*. One particular MRI sequence is chosen depending on the target of medical examination, the examined body part, available measurement duration, and scanner capabilities.

Data acquired throughout the MRI measurement sequence, encoded via frequency and phase, can be represented as a set of complex-valued data points in k -space. The measurement sequence defines the amount of data points and their position in k -space, often called a *k -space trajectory*. In the present work the sampling in the Cartesian grid in three-dimensional k -space is considered.

For a three-dimensional acquisition of a spatially resolved quantity $\rho(x, y, z)$, the MRI measured signal s can be formulated as follows

$$s(k_x, k_y, k_z) = \int \int \int \rho(x, y, z) e^{-i2\pi(k_x x + k_y y + k_z z)} dx dy dz = \mathcal{F}[\rho(x, y, z)], \quad (2.17)$$

with \mathcal{F} being a Fourier transform.

And for a real-world measurement with finite number of acquisition steps N, M, L along each of x, y and z dimensions and a finite Field Of View (FOV)

$$S(k_x, k_y, k_z) = \sum_{n=-N/2}^{N/2-1} \sum_{m=-M/2}^{M/2-1} \sum_{l=-L/2}^{L/2-1} \rho(x, y, z) e^{-i2\pi(n\Delta k_x + m\Delta k_y + l\Delta k_z)} = \mathbf{F}[\rho(x, y, z)], \quad (2.18)$$

with \mathbf{F} being a Discrete Fourier Transform (DFT) and Δk_i being a reciprocal of FOV_i along the

axis $i \in \{x, y, z\}$.

And, consequently, for the reconstruction I of the ρ from the measured $s(k_x, k_y, k_z)$ an inverse Fourier transform \mathbf{F}^{-1} can be applied.

$$I(x, y, z) = \mathbf{F}^{-1}[s(k_x, k_y, k_z)] \approx \rho(x, y, z) \quad (2.19)$$

Typically, a single acquisition measurement samples a complete line (this dimension called a *readout direction*) of data points in k -space rather than a single data point.

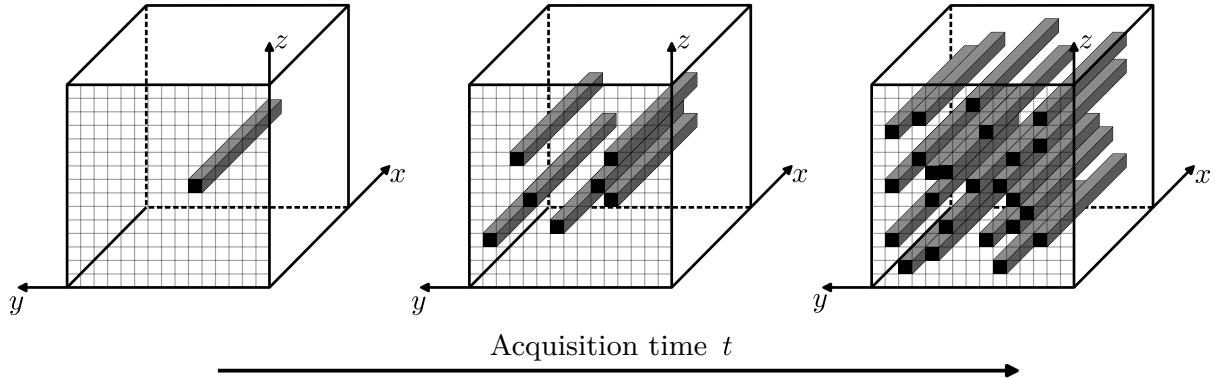


Figure 2: Sampling in Cartesian three-dimensional k -space of shape $N \times M \times L \text{ px}^3$. The x -axis corresponds to the readout direction. The FOV-limited volume is sampled line by line throughout the acquisition.

Since the measurement time for each line along the readout dimension is fixed, the overall duration of an acquisition is limited by the number of lines sampled in the three-dimensional space and can only be accelerated by reducing the number of sampling lines in the space.

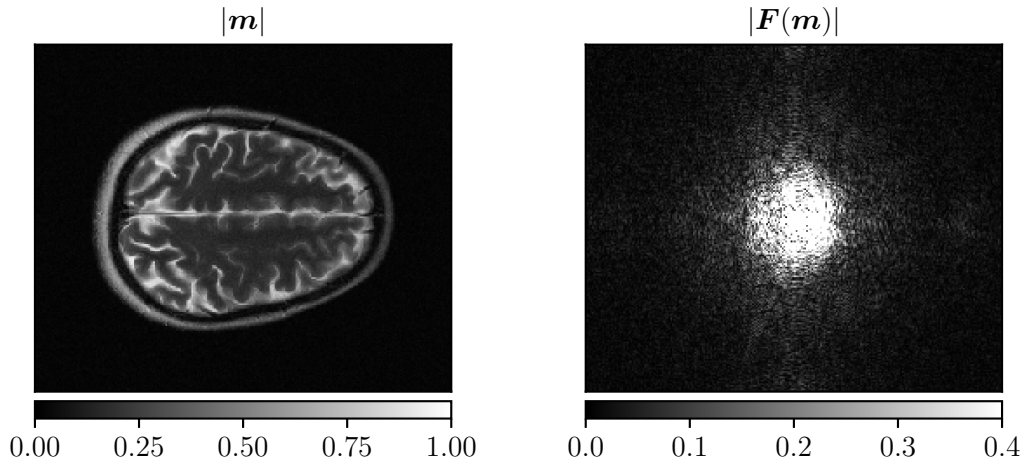


Figure 3: Sample slice of the brain (left) and its DFT (right). The signal intensity in the central part of the k -space is the highest and decreases toward the periphery region.

The distribution of the signal strength for an anatomical structure is highly non-uniform across the k -space. For example magnitudes of a brain acquisition $|\mathbf{m}|$ and corresponding Fourier Transform $|\mathbf{F}(\mathbf{m})|$, shown in Figure 3, demonstrate that the most intense signal amplitude is localised in the central area of k -space and declines towards the periphery.

Spatial distribution of the signal in k -space is directly related to the spatial information of

acquisition content. Lower spatial frequencies, closer to the centre of k -space, correspond to larger features in image domain and encode the global image contrast and coarse structures. Higher spatial frequencies, lying far from the centre of k -space, correspond to fine structural details and sharper image.

Measurement in MRI is accompanied with the noise arising both from the specimen, receiver coils and electronical hardware. This noise is generally assumed to be normally distributed and frequency-independent [33] in real and imaginary parts of the measured data. This means that the higher frequency signal of lower strength naturally has lower Signal-to-Noise Ratio (SNR), and depending on the ration of the measurement signal to the noise amplitude (especially in the ULF MRI) measurement of higher frequencies can be very complicated.

Different strategies for the choice of k -space trajectory are present. Especially, for the acceleration of the measurement via reducing amount of sampled data values without a significant loss in acquisition quality and resolution is a common problem.

For example, common approaches are the trajectories with higher density of the sampled data values in the k -space centre (for example with density proportional to the Gaussian distribution), or Partial Fourier (PF) sampling where as little as one-half of k -space is sampled, exploiting rather slow natural phase change in the MRI acquisitions and conjugate symmetry of k -space.

2.1.4 Single- and multi-coil acquisitions

In MRI, data can be acquired using a single RF coil or an array of multiple coils. Single-coil acquisitions are conceptually straightforward. Application of multiple coils has become the standard in modern MRI systems due to the improved SNR and the possibility of accelerated parallel imaging.

In multi-coil acquisitions, each coil receives the measurement RF signal but have varying sensitivity profiles, meaning that the measured signal from each coil is modulated by its corresponding coil sensitivity. Consequently, the reconstruction of a single image from multi-coil data requires Coil Sensitivity Maps (CSMs), which characterises the signal response of each coil.

The CSMs are often determined with special calibration sequences before the actual examination but can be evaluated on the basis of the acquired k -space data. There are numerical algorithms designed for the CSM reconstruction. The most commonly used algorithms are Inati [34], Walsh [35] and ESPIRiT [36].

For k -space data acquired with n coils, vector \mathbf{m}^k of length n denotes the measurement data and vector \mathbf{c} being the known vector CSMs with the same length n . The corresponding complex-valued image $\hat{\mathbf{u}}$ can then be reconstructed as

$$\hat{\mathbf{u}} = \frac{1}{\|\mathbf{c}\|_2} \sum_{i=1}^n \mathbf{c}_i^* \cdot \mathbf{F}(\mathbf{m}_i^k), \quad (2.20)$$

with \mathbf{c}^* being a complex conjugate of \mathbf{c} and $\|\cdot\|_2$ being a L^2 -norm.

2.2 General reconstruction problem

The forward problem of a MRI acquisition can be posed as follows

$$\mathbf{m}^k = \mathbf{A}\mathbf{u}_{\text{true}} + \mathbf{n}, \quad (2.21)$$

where \mathbf{A} being an acquisition model operator, \mathbf{u}_{true} being the unknown original data, \mathbf{n} being a statistical noise and \mathbf{m}^k being the k -space data acquired with the measurement.

In general, this problem ill-posed inverse problem which is not exactly solvable for the \mathbf{u}_{true} due to unknown noise \mathbf{n} . Therefore, the problem is often reformulated to maximise likelihood estimation of \mathbf{m}^k and \mathbf{u} which leads to the least-squares problem for \mathbf{u} :

$$\mathbf{u}_0 = \arg \min_{\mathbf{u}} \left\| \mathbf{A}\mathbf{u} - \mathbf{m}^k \right\|_2^2, \quad (2.22)$$

where $\|\cdot\|_2$ being the L^2 -norm.

The minima is determined by setting the derivative of the functional on the right-hand side in respect to \mathbf{u} to zero:

$$\begin{aligned} \frac{\partial}{\partial \mathbf{u}} \left\| \mathbf{A}\mathbf{u} - \mathbf{m}^k \right\|_2^2 &= 0 \\ \Rightarrow \mathbf{A}^H(\mathbf{A}\mathbf{u} - \mathbf{m}^k) &= \mathbf{A}^H\mathbf{A}\mathbf{u} - \mathbf{A}^H\mathbf{m}^k = 0 \end{aligned} \quad (2.23)$$

with \mathbf{A}^H being an adjoint operator to an operator \mathbf{A} .

This gives the following equation for the unknown \mathbf{u}_0

$$\mathbf{A}^H\mathbf{A}\mathbf{u}_0 = \mathbf{A}^H\mathbf{m}^k \quad (2.24)$$

and has the following general form solution

$$\mathbf{u}_0 = (\mathbf{A}^H\mathbf{A})^{-1}\mathbf{A}^H\mathbf{m}^k \quad (2.25)$$

The general Equation 2.22 can be extended with the so-called *regularisation term* $\mathcal{R}(\mathbf{u})$ to incorporate prior knowledge properties about the \mathbf{u} .

$$\mathbf{u}_0 = \arg \min_{\mathbf{u}} \left\{ \frac{1}{2} \left\| \mathbf{A}\mathbf{u} - \mathbf{m}^k \right\|_2^2 + \frac{\lambda}{2} \mathcal{R}(\mathbf{u}) \right\}, \quad (2.26)$$

with λ being a non-negative scalar value. The value λ acts as a weighting of regularisation term's impact in respect to the first term, often called *data consistency* term. Choice of the regularisation term is strongly dependent from the reconstruction problem statement. Often used are the Total Variation (TV) [37, 38], wavelet transformation [39], or an externally predicted prior (for example, prediction of a DL model) [40–42].

Regularisation term $\mathcal{R}(\mathbf{u})$ defined by an externally predicted solution \mathbf{u}_r is posed as follows:

$$\mathcal{R}(\mathbf{u}) = \left\| \mathbf{u} - \mathbf{u}_r \right\|_2^2 \quad (2.27)$$

For this particular form of regularisation term, solution for Equation 2.26 becomes

$$\begin{aligned} \frac{\partial}{\partial \mathbf{u}} \left(\frac{1}{2} \left\| \mathbf{A}\mathbf{u} - \mathbf{m}^k \right\|_2^2 + \frac{\lambda}{2} \left\| \mathbf{u} - \mathbf{u}_r \right\|_2^2 \right) &= 0 \\ \Rightarrow \mathbf{A}^H(\mathbf{A}\mathbf{u} - \mathbf{m}^k) + \lambda(\mathbf{u} - \mathbf{u}_r) &= \mathbf{A}^H\mathbf{A}\mathbf{u} - \mathbf{A}^H\mathbf{m}^k + \lambda\mathbf{u} - \lambda\mathbf{u}_r \\ = (\mathbf{A}^H\mathbf{A} + \lambda\mathbf{I})\mathbf{u} - \mathbf{A}^H\mathbf{m}^k - \lambda\mathbf{u}_r &= 0 \end{aligned} \quad (2.28)$$

and yields the following Equation for the unknown \mathbf{u}

$$(\mathbf{A}^H \mathbf{A} + \lambda \mathbf{I}) \mathbf{u} = \mathbf{A}^H \mathbf{m}^k + \lambda \mathbf{u}_r \quad (2.29)$$

This equation is consistent with Equation 2.24 and reduces to the same form when the regularisation weight $\lambda = 0$.

The equation for \mathbf{u} in form of $\mathbf{Wu} = \mathbf{c}$ can generally be solved numerically, for instance using the conjugate gradient method, while depending on the operator \mathbf{A} , a closed-form solution for \mathbf{u} may exist.

2.3 Deep-Learning model

2.3.1 Artificial neural network

An Artificial Neural Network (ANN) consists of a sequential composition of multiple functional elements (*layers*). The first (top) and last (bottom) layers are called input and output layers, respectively.

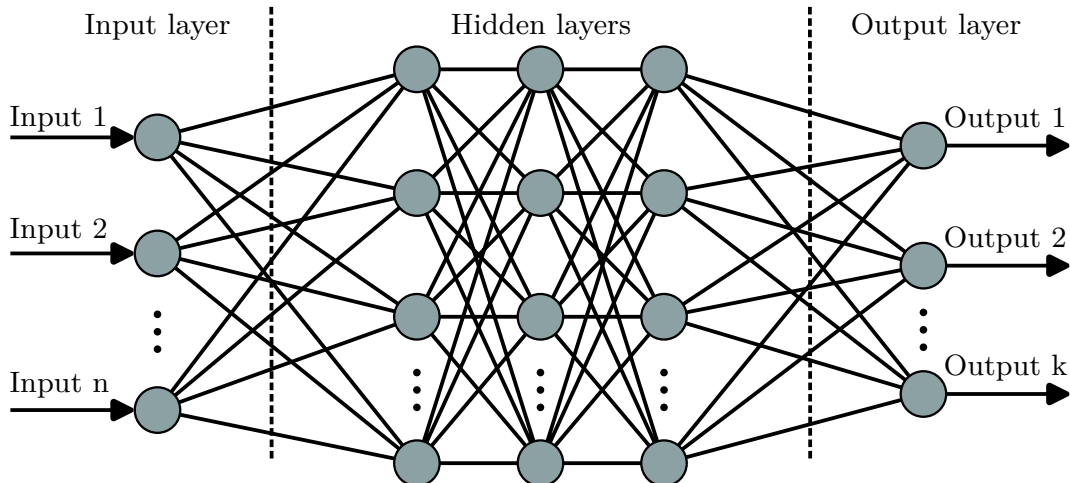


Figure 4: Schematic representation of an trivial ANN with input layer as vector of length n inputs and output layer as vector of length k .

An input and output of a layer can be a tensor of an arbitrary shape. Each layer represents a mathematical operation and can have a set of variables w (*learnable parameters* or *hyperparameters*). The connection between layers can be direct or passed through a special function (*activation function*) to introduce a non-linear response of the network. Then, a defined sequence of various layers and activation functions is called *model*.

Training of a model is the process of modification of learnable parameters to minimise the value of a function \mathcal{L} called *loss function*. In case of *supervised learning* the loss function $\mathcal{L}(\hat{y}^{(i)}, y^{(i)})$ takes the return value of the output layer $\hat{y}^{(i)} = M(x^{(i)}; w)$ and a corresponding Ground Truth (GT) $y^{(i)}$ as arguments. A set of pairs $\mathcal{D} = \{(x^{(i)}, y^{(i)})_{i=1}^N\}$ of input data $x^{(i)}$ and a corresponding GT $y^{(i)}$ of length N is called a *dataset*.

The supervised learning training procedure can be formulated as an iterative algorithm as shown in Algorithm 1.

Algorithm 1 Supervised Learning Algorithm for an ANN

Require: Model M , Loss function \mathcal{L} , Training data $\mathcal{D} = \{(x^{(i)}, y^{(i)})\}_{i=1}^N$, Parameters state w , Batch size B , Learning rate η , Number of epochs E

- 1: **for** epoch = 1 to E **do**
- 2: **for** each training batch $\{(x^{(n)}, y^{(n)})\}_{n=1}^B \subset \mathcal{D}$ **do**
- 3: **Forward pass:** Compute predictions $\{\hat{y}^{(n)}\}_{n=1}^B := M(\{x^{(n)}\}_{n=1}^B; w)$
- 4: **Compute loss:** $L := \sum_n^B \mathcal{L}(\hat{y}^{(n)}, y^{(n)})$
- 5: **Backward pass:** Compute gradients $\nabla_w L$
- 6: **Update parameters:** $w \leftarrow w - \eta \cdot \nabla_w L$
- 7: **end for**
- 8: **end for**

The prediction $\hat{y}^{(i)}$ of a trained model M with parameter state w is obtained following the trivial algorithm:

Algorithm 2 Supervised learned model prediction

Require: Model M , Parameters state w

- 1: **Input:** $x^{(i)}$
- 2: **Predict:** $\hat{y}^{(i)} := M(x^{(i)}; w)$
- 3: **return** $\hat{y}^{(i)}$

With a training algorithm as a problem of searching local minima of the loss function in a multidimensional space, often a gradient descent method is applied, with a *learning rate* as a ratio for a step size in approaching of the local minima. Setting to the learning rate to high would not allow to approach local minima by bouncing back and forth, while a too small learning rate set would consume too much time.

Number of steps (*epochs*) for optimization of model parameters w is a trade-off between the training duration and proximity to the model local minima. The exact choice of the number of epochs depends on the model size and learning rate. Typically, an abrupt decay of the loss function at the preliminary training steps and very slow asymptotically approaching the local minima is observed.

In order to stabilise the approach to the local minima in the trainable parameters steps and allow the model to deliver a more generalised result among the training data, model parameters optimization is performed not for a single pair of the data, but for a set of training data pairs (*batch*) of length B (*batch size*), being a subset of dataset \mathcal{D} .

A common issue for the large models is the case when instead of generalization of the problem, the large model can be unintentionally optimized in a way to memorize all outcomes for the pairs in training dataset. To prevent a model to "memorize" all expected outcomes (*overfit*) for each of training input and ground truth pair, training is performed for two different *training* and *evaluation* datasets. Evaluation of a trained model efficiency is performed with the third *test* dataset consisting of the pairs which have never appeared in the training phase for the given model.

2.3.2 Convolutional neural networks

Convolutional Neural Networks (CNNs) represent a special class of ANNs that predominantly consists of multiple convolutional layers composed of kernels of various shapes, with values of the kernels being trainable parameters. Modification of kernel values allows to extract relevant structural features of an input. Moreover, consequent connection of convolution layers allows to increase the complexity of the extracted features based on output of previous layers and propagate them throughout the model.

CNNs gained their popularity in the past decades and became a common approach for computer vision and image processing problems and for inverse problems, as MRI reconstruction as well [43].

Common applications of CNNs in context of MRI reconstruction problem are points, outlined in the previous Chapter, such as: suppression of the statistical noise (*denoising*), recovery of higher resolved data with the lower resolved measurement (*super-resolution*), and reconstruction of accelerated measurements partially sampled in k -space (*undersampling*).

Among other subclasses of CNNs, the Residual Channel Attention Network (RCAN) model [44] and its slightly modified model [24], successfully applied and demonstrated good results in benchmarks for the denoising and super-resolution problems of the three-dimensional ULF MRI brain acquisitions, as well as of undersampled acquisition.

The model consists of the cascade of the Residual Groups (RGs) with modified Residual Channel Attention Blocks (mRCABs), then concatenated with the mRCABs as shown in Figure 5 RG and Channel Attention (CA) blocks, which

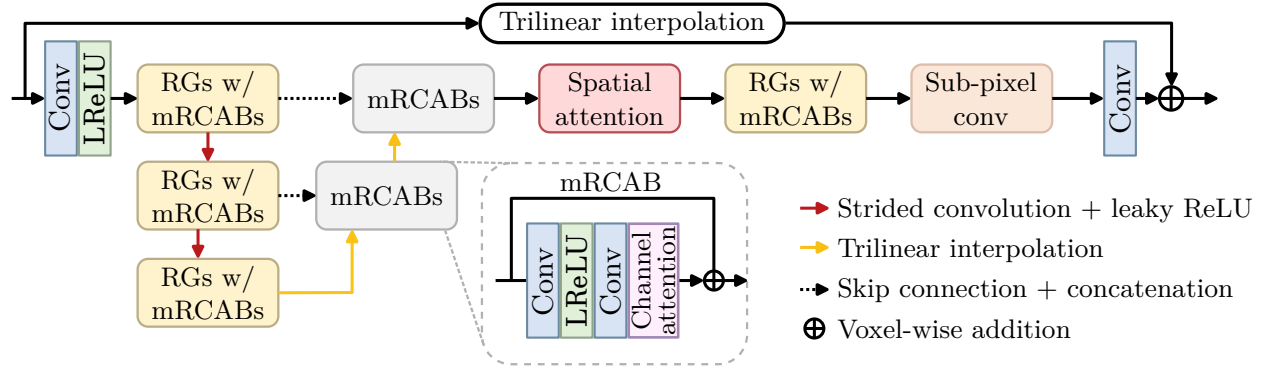


Figure 5: Schematic representation of the RCAN model architecture published in [24].

Due to the similarity of the tasks expected for the model performance, this model was taken as a basis for the model proposed in the next section.

2.3.3 Complex valued network approach

In most applications of machine learning models to MRI reconstruction, CNNs act in the magnitudes image domain. This is dominantly motivated by the fact that the magnitude images are only relevant for clinical diagnostics.

However, this approach neglects the complex-valued nature of the MRI signal, where both real and imaginary components carry physical information. An approach of fully complex-valued neural networks, where both complex-valued trainable parameters w and input data are represented as

complex values, was demonstrated earlier [45] but did not become common in the research field due to the mathematical and computational complexity.

Nevertheless, only a limited set of applications [46] or retrieval of the B_0 field would require the complex-valued signal. This would also be essential for the consistency with the MRI reconstruction problem and acquisition operator (see Equation 2.29) for the development of physics-informed model. In addition, even when the model is developed to deliver better results for magnitude images, the model may still benefit from the complex-valued input, since the complex-valued information can provide more signal-related constraints.

In the present work the complex valued network was implemented by the representation of imaginary and real part as two independent real-valued channels in a similar way as a digital colour image is represented in three (red, green and blue) channels.

The naive implementation of the complex-valued network with the complex-valued trainable parameters, complex-valued inputs, and special complex-valued activation functions did not work as intended and did not allow the network to converge over the training steps to deliver sensible results.

Since real and imaginary channels are not restricted to positive values only, as magnitudes do, the activation functions of the original network above were exchanged with the odd activation functions to achieve symmetric behaviour with respect to zero.

Another possible approach is to represent the complex values as two separate channels of magnitudes and the phase portrait. However, this representation makes the channels to have completely different meaning, which would make less sense to process them through a single model.

2.4 Challenges of low-field MRI system

The MRI systems can be divided into groups by the strength of the magnetic field B_0 in the Low-Field (LF) (less than 1.5 T), High-Field (HF) (1.5 to 3 T) and Ultra-High-Field (UHF) (7 T and above). Under the LF systems special group under 50 mT can be considered as ULF system.

The ULF MRI systems are not intended to compete to LF or HF MRI systems and serving a complementary role making MRI accessible for world population, rapid screening, for example as brain examination, and portable. These goals also impose limits on the hardware equipment what affects the acquisition SNR.

In this work I would focus on the in-house developed open-source OSI² ONE prototype ULF MRI system [47] with B_0 strength of 50 mT.



Figure 6: Photo of (left) assembled the OSI² ONE MRI system and (right) stand-alone Halbach array magnet chamber.

Main challenge of the ULF MRI system is significantly lower acquisition SNR, compared to conventional HF MRI, due to the orders of magnitudes weaker B_0 field. In order to ensure sufficient SNR within a clinically feasible acquisition time, the spatial resolution of the ULF MRI is much lower than conventional scanners have.

In context of the present thesis, absence of the large dataset acquired with the ULF MRI is most challenging. Often DL models are trained with a dataset of paired ULF and HF MRI acquisitions [48]. This is not the case for the OSI² ONE scanner due to multiple reasons, such as current lack of clearance for patient use and insufficient time for dataset collection.

3 Image-base super-resolution and denoising

3.1 Introduction

The Ultra-Low-Field (ULF) in-house developed Magnetic Resonance Imaging (MRI) system [12] aims to make the MRI diagnostic tool mobile, accessible, and affordable. However, such systems are not able to compete with large-scale machines in terms of Signal-to-Noise Ratio (SNR) due to numerous hardware limitations such as a much weaker static magnetic field.

Thus, in order to achieve an acquisition quality for diagnostic interpretation, there is a trade-off between acquisition SNR, scan duration, and spatial resolution. Provided that the scan duration is limited by natural factors and the ULF MRI project aims for rapid screening application with a total acquisition time of approximately ten minutes, an increase in acquisition SNR under fixed scan duration is achievable only with a reduced acquisition resolution.

Convolutional Neural Networks (CNNs) has already demonstrated capable for mitigation of the noise and increasing resolution for the MRI reconstruction problem especially for Low-Field (LF) and ULF MRI systems [22–26]. The proposed Deep-Learning (DL) models predict an output with increased resolution (*super-resolution*) and reduced noise (*denoising*). The models act in the magnitudes domain, assigning a high-resolution, low-noise magnitude image to a low-resolution magnitude image with a lower SNR.

A novel approach, which I propose in this Chapter, is an Residual Channel Attention Network (RCAN) DL model, acting in the complex-valued domain. The developed model predicts a complex-valued image with higher spatial resolution and reduced noise for a complex-valued MRI image input. The main motivation for developing a complex-valued model are potential benefits of exploiting additional phase information, missing in the conventional magnitudes domain approaches, for better super-resolution and denoising tasks, as well as being an intermediate step in development of a physics-informed model framework, where the complex-valued data is essential. Also, a complex-valued MRI denoised image is required for applications which are particularly relevant for an ULF MRI, as estimation of B_0 field inhomogeneities [28].

The development of the complex-valued model requires preparation of a training dataset, composed of paired low-resolution, low SNR and high-resolution, high SNR complex-valued images. Due to the absence of large publicly available datasets of ULF MRI acquisitions, two complex-valued training datasets were prepared. The datasets are based on the publicly available fastMRI [49] dataset of High-Field (HF) MRI acquisitions, but had two completely different approaches for generation of phase information.

As part of the experiment described in this Chapter, various configurations of the complex-valued model were evaluated to determine the model, which achieves the best performance in terms of image quality metrics for the models' predictions. The models are also examined against a baseline reconstruction and the reference model of a similar architecture, which acts in the magnitudes domain only.

3.2 Methods

3.2.1 Deep-Learning models implementation

A DL model for the experiments was intended to match RCAN-like architecture, proposed in [24]. The model was implemented in PyTorch [50] framework* and was designed to have adjustable configuration for input and output shapes, including spatial dimensions and amount of channels.

The magnitudes DL model represents a particular case of this basic model with a single input and output channel and is referred to as $\text{RCAN}_{\mathbb{R}}$. The complex-valued DL model uses an identical configuration, except with two input and output channels, and is denoted as $\text{RCAN}_{\mathbb{C}}$.

3.2.2 Training dataset preparation

For supervised learning of a model (Algorithm 1) pairs of inputs and Ground Truth (GT) data $(x^{(i)}, y^{(i)})$ are required. Application of the data measured with the ULF system is not possible since the fundamental GT cannot be recovered by measurement. Often used pairs of the ULF and HF MRI paired acquisitions also not publicly available and cannot be acquired for project dedicated time. Currently, the ULF MRI prototype at PTB is not cleared for patient use.

Therefore, the experimental dataset bases on the publicly available fastMRI [49] dataset consisting of 2526 T_2 weighted brain acquisitions obtained with commercial 3 T scanners in high resolution with the noise level far below the noise level of ULF MRI. The brain acquisitions are available as both fully sampled Cartesian multi-coil k -space raw data and the corresponding magnitude images obtained by the vendor reconstruction. The T_2 weighted acquisitions are considered since the T_2 weighted contrast is less influenced by the strength of B_0 and therefore can be better transferred to ULF MRI.

Reconstructed ground truth dataset $\mathcal{D}_{\text{walsh}}$

Since no Coil Sensitivity Maps (CSMs) are provided within the fastMRI dataset, the CSMs are calculated with implementation of Walsh algorithm from the MRpro software package [51] based on the multi-coil k -space data of the acquisitions.

Then, composed complex-valued acquisitions were reconstructed according to Equation 2.20 with the both of CSMs.

The complex-valued images reconstructed with the CSMs, provided by Inati algorithm, were dominantly real-valued with a much lower imaginary part of the recovered complex-valued acquisition, which can be explained by design of the Inati algorithm.

The goal of preparing a dataset from k -space data is to obtain complex images that are most similar to the acquisitions made with the ULF MRI system. Thus, the CSMs retrieved with Inati algorithm were not used for training. The dataset of complex-valued reconstruction retrieved with Walsh algorithm estimated CSMs indicated a much more similar phase portrait to the acquisitions made with the original ULF MRI system and was used for experiments.

Then, the complex-valued three-dimensional acquisitions were scaled to the shape of $16 \times 200 \times 240$ via the nearest-neighbour interpolation algorithm and represent the GT $y^{(i)}$ of the $\mathcal{D}_{\text{walsh}}$ dataset.

*model implementation available at <https://github.com/lrlunin/high-res-low-field-mri>

Simulated ground truth dataset \mathcal{D}_{sim}

The second dataset \mathcal{D}_{sim} was prepared using the vendor reconstructed magnitude images y provided in the fastMRI dataset and the simulated phase component φ . Firstly, the magnitude images were scaled to the identical shape of $16 \times 200 \times 240$ via the nearest-neighbour interpolation algorithm and normalised from 0 to 1 as follows:

$$\bar{y} = \frac{y - \min(y)}{\max(y) - \min(y)} \quad (3.1)$$

The phase component φ was simulated as a linear slope in x - y plane of a three-dimensional space, exceeding π rad in the centre of the image, accompanied with a slow linear increase of phase angle along the z -axis. Orientation of a phase front in x - y plane was chosen randomly in range of 0 to 360° for each of GT data $y^{(i)}$ in the dataset. The global phase shift was chosen randomly in range of $-\frac{\pi}{3}$ to $+\frac{\pi}{3}$ rad for each of GT data $y^{(i)}$ in the dataset.

Then, complex-valued GT data $y^{(i)}$ was obtained by element-wise multiplication of the magnitude data \bar{y} with the phase component φ :

$$y_{ijk}^{(i)} = \bar{y}_{ijk} e^{i\varphi_{ijk}} \quad (3.2)$$

Simulation of ULF MRI acquisitions

For the simulation of data acquired with the ULF MRI, which represent the model input $x^{(i)}$, the following chain of operators was applied to the GT data $y^{(i)}$ of both \mathcal{D}_{walsh} and \mathcal{D}_{sim} datasets:

$$x^{(i)} = \mathbf{F}^{-1}(\mathbf{D}\mathbf{F}y^{(i)} + \mathcal{N}(0, \sigma^2)), \quad (3.3)$$

with $\mathbf{D} : \mathbb{C}^{16 \times 200 \times 240} \rightarrow \mathbb{C}^{16 \times 100 \times 120}$ is k -space downsampling operator, sampling only the central part of k -space and σ^2 randomly selected in range of 0.03 to 0.06 to simulate the acquisition noise of ULF MRI. Randomness of the noise variance over the acquisition series should prevent the model to eliminate only the one specific level of noise.

Magnitudes dataset \mathcal{D}_{mag}

For the experiments with the model acting in the magnitudes domain, dataset consisting of acquisition magnitudes, further denoted as \mathcal{D}_{mag} , was constructed.

To ensure consistency with previously prepared complex-valued datasets, the input and GT pairs $\{(x^{(i)}, y^{(i)})\}$ of the dataset \mathcal{D}_{mag} are calculated as magnitudes of input $|x^{(i)}|$ and GT $|y^{(i)}|$ pairs of the \mathcal{D}_{sim} dataset.

3.2.3 Super-resolution and denoising problem

Training of the models was performed as supervised learning (Algorithm 1). The complex-valued model, further denoted as $\text{RCAN}_{\mathbb{C}}$, was trained on both \mathcal{D}_{walsh} and \mathcal{D}_{sim} datasets, with two different loss functions \mathcal{L}_c and \mathcal{L}_m .

The first loss function \mathcal{L}_c is the difference of imaginary and real channels of the prediction $\hat{y}^{(i)}$

and corresponding GT data $y^{(i)}$

$$\mathcal{L}_c(\hat{y}^{(i)}, y^{(i)}) = |\Re(\hat{y}^{(i)}) - \Re(y^{(i)})| + |\Im(\hat{y}^{(i)}) - \Im(y^{(i)})|, \quad (3.4)$$

with $\Re(\cdot)$ and $\Im(\cdot)$ being the real and imaginary components of the complex-valued data. This loss function sets the training objective as the minimisation of difference between individual real and imaginary parts of complex-valued data.

The second loss function \mathcal{L}_m is the difference of the magnitudes of the prediction $\hat{y}^{(i)}$ and corresponding GT data $y^{(i)}$

$$\mathcal{L}_m(\hat{y}^{(i)}, y^{(i)}) = ||\hat{y}^{(i)}| - |y^{(i)}|| = \left| \sqrt{\Re^2(\hat{y}^{(i)}) + \Im^2(\hat{y}^{(i)})} - \sqrt{\Re^2(y^{(i)}) + \Im^2(y^{(i)})} \right| \quad (3.5)$$

This loss function sets the training objective as the minimisation of difference between the magnitudes, resulting from the real and imaginary parts of complex-valued data. This objective, however, does not imply the minimal difference between of real and imaginary components.

The reference DL model, acting in the magnitudes domain, further denoted as $\text{RCAN}_{\mathbb{R}}$, is trained on dataset \mathcal{D}_{mag} with the loss function

$$\mathcal{L}_1(\hat{y}^{(i)}, y^{(i)}) = |\hat{y}^{(i)} - y^{(i)}|, \quad (3.6)$$

setting the training objective as the minimisation of difference between the magnitudes.

3.3 Experiments

3.3.1 Super-resolution and denoising problem

Model configurations

Each of prepared datasets \mathcal{D}_{walsh} , \mathcal{D}_{sim} and \mathcal{D}_{mag} of 2526 data pairs $(x^{(i)}, y^{(i)})$ are split in three sub-datasets of pairs: training, validation and test datasets, each having 1768, 506 and 252 data pairs, respectively. The $\text{RCAN}_{\mathbb{C}}$ and $\text{RCAN}_{\mathbb{R}}$ models had a comparable number of trainable parameters of 3 778 970 and 3 776 809. The learning rate for training for all models is set to 1×10^{-4} , batch size is set to 8, optimiser is AdamW, and number of training epochs is set to 120. Training was performed on a single NVIDIA A100 GPU and lasted approximately 5 hours for each model to train.

In total, 5 models were trained. Four complex-valued models $\text{RCAN}_{\mathbb{C}}$ were trained by evaluating all combinations of two datasets $\{\mathcal{D}_{sim}, \mathcal{D}_{walsh}\}$ and two loss functions $\{\mathcal{L}_c, \mathcal{L}_m\}$. The one magnitude model $\text{RCAN}_{\mathbb{R}}$ was trained on \mathcal{D}_{mag} dataset and with \mathcal{L}_1 loss function.

As a baseline reference, the magnitudes of inverse Fourier transform of zero-padded input $x^{(i)}$ in k -space, further denoted as "zero-pad baseline", were taken.

Model performance benchmark

For performance evaluation of trained models, the image quality metrics are applied to the pairs of prediction and GT $(\hat{y}^{(i)}, x^{(i)})$ of the test sub-datasets. The following metrics are used: Structural

Similarity Index Measure (SSIM) with three-dimensional cubic Gaussian kernels of $3 \times 3 \times 3 \text{ px}^3$, Mean-Squared Error (MSE) and Peak Signal-to-Noise Ratio (PSNR).

For the complex-valued models $\text{RCAN}_{\mathbb{C}}$, the metrics were evaluated for both individual real and imaginary channels, and the resulting magnitudes. For the magnitude model $\text{RCAN}_{\mathbb{R}}$, only the metrics for magnitudes were evaluated.

In each x - y slice, an area of brain region is comparable to that of the background. This imbalance between the brain and background regions is particularly pronounced in the upper slices along the z -axis.

Thus, an application of the metrics to the whole volume, with each of voxel contributing equally to the general score of a metric, would be unintentionally biased towards the background similarity and do not represent a brain structure similarity but the averaged of both brain and background similarity.

In order to establish a better benchmark, set of rectangular binary masks enclosing the brain region each of the x - y slice each of GT data $y^{(i)}$ of the test sub-dataset were generated, exemplarily shown in Figure 7. Metric results are evaluated only within the volumes enclosed by the generated masks.

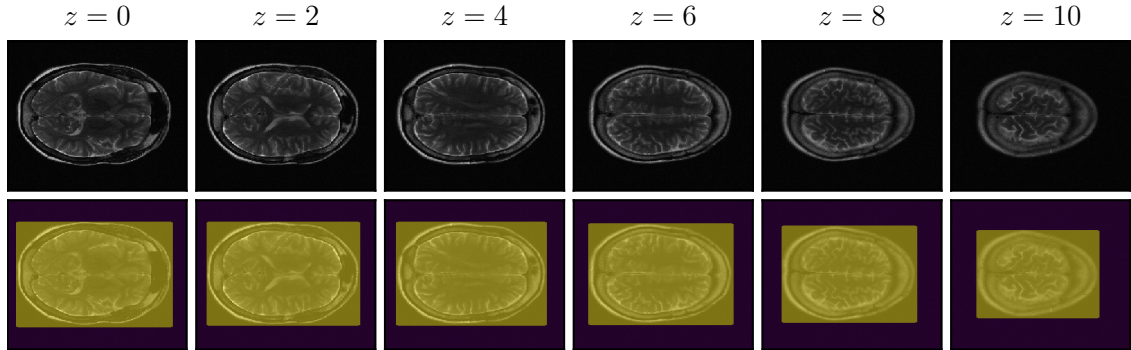


Figure 7: Particular slices along the z -axis of the example three-dimensional data from the test dataset (upper row) w\o and (bottom row) w\ rectangular binary masks. The yellow rectangular area correspond to the value of one, the area outside of yellow rectangular is zero.

3.4 Results

3.4.1 Training dataset preparation

The same image from the datasets is shown in Figure 8 with the same resulting GT magnitude image $|y^{(i)}|$ a phase obtained with the Walsh reconstruction algorithm and completely simulated phase portraits are depicted in the bottom row. With the Gaussian noise $\mathcal{N}(0, \sigma^2)$ in both real and imaginary channels the $|x^{(i)}|$ has a noise following the Rayleigh distribution with the variance of $\left(2 - \frac{\pi}{2}\right) \sigma^2$ and mean of $\sigma \sqrt{\frac{\pi}{2}}$.

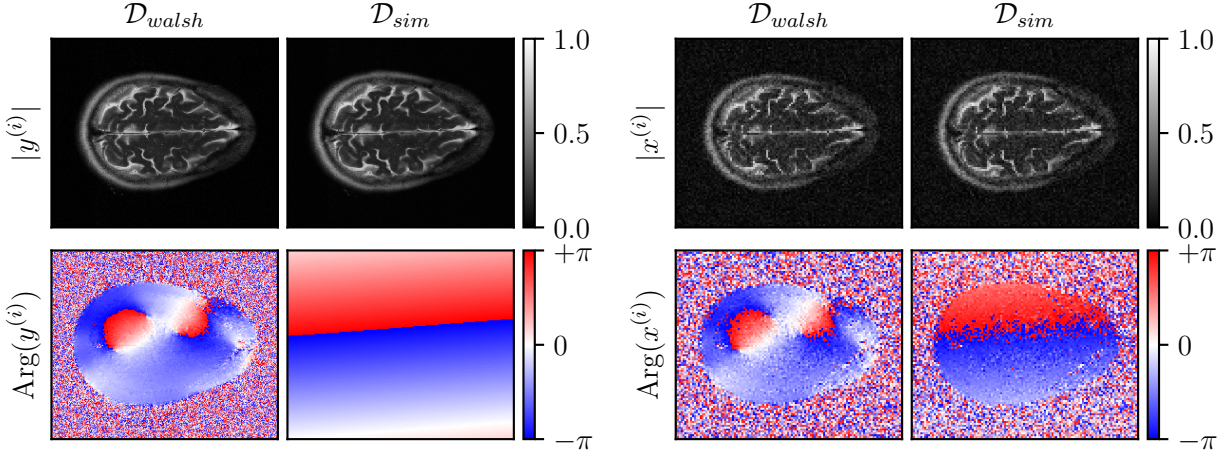


Figure 8: (left) GT $y^{(i)}$ and (right) inputs $x^{(i)}$ of (top) magnitudes and (bottom) argument angle of complex-valued data.

3.4.2 Super-resolution and denoising problem

For each of input data $x^{(i)}$ of test sub-dataset, predictions $\hat{y}^{(i)}$ with each of 5 trained models were made. The test sub-dataset was selected from the same dataset as the training sub-dataset used for evaluated model. Then, the image quality metrics were evaluated on pairs of models predictions $\hat{y}^{(i)}$ and GT data $y^{(i)}$.

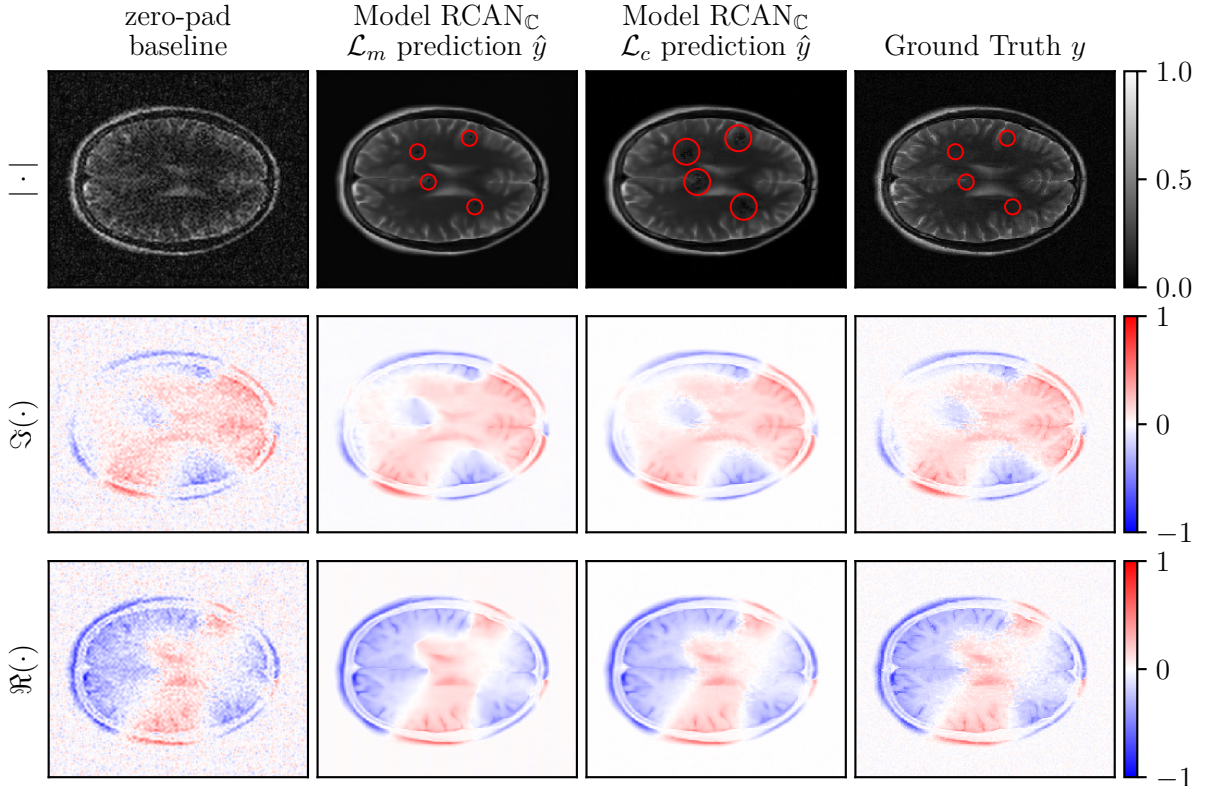


Figure 9: Exemplarily selected x - y slice of data \mathcal{D}_{walsh} with baseline zero-pad reconstruction, predictions of RCAN_C models trained with different loss functions and corresponding GT. Areas with image artifacts present in the RCAN_C models predictions but absent in the GT are highlighted with red circles.

In Figure 9 a single x - y slice of the $\text{RCAN}_{\mathbb{C}}$ model trained on the train sub-dataset of $\mathcal{D}_{\text{walsh}}$ with two loss functions is shown, as well as the zero-pad baseline and corresponding GT. While both of the $\text{RCAN}_{\mathbb{C}}$ models trained with \mathcal{L}_m and \mathcal{L}_c are capable to solve denoising and super-resolution problems, they both produce hole-like artifacts in the predictions.

The x - y slice corresponding to that shown in Figure 9, was taken from \mathcal{D}_{sim} and evaluated using the $\text{RCAN}_{\mathbb{C}}$ model trained on \mathcal{D}_{sim} , with the resulting predictions shown in Figure 10.

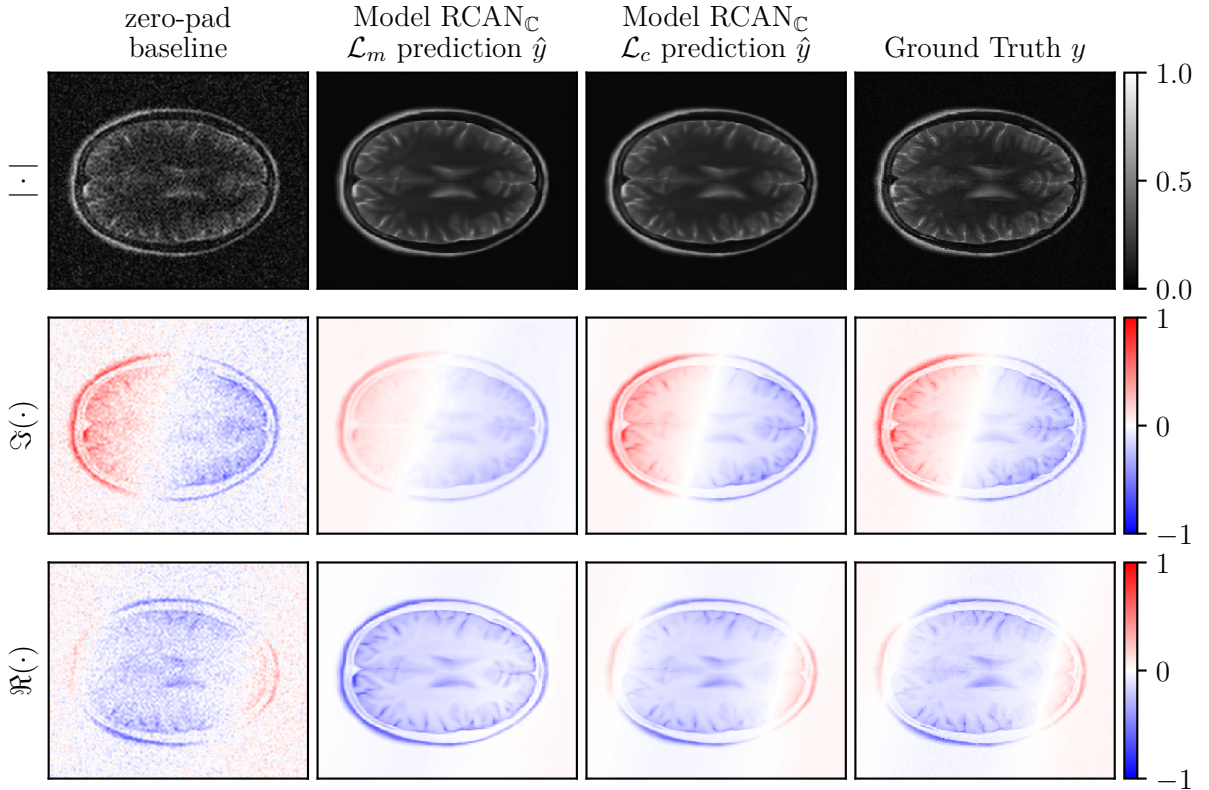


Figure 10: Exemplarily selected x - y slice of data \mathcal{D}_{sim} with baseline zero-pad reconstruction, predictions of $\text{RCAN}_{\mathbb{C}}$ models trained with different loss functions and corresponding GT. Clearly visible is a wrong reconstruction of real and imaginary parts for prediction of $\text{RCAN}_{\mathbb{C}}$ model trained with \mathcal{L}_m loss function.

Models trained on the \mathcal{D}_{sim} are capable to predict denoised magnitudes images of increased resolution, without producing visible artifacts. However, the $\text{RCAN}_{\mathbb{C}}$ model trained with the \mathcal{L}_m loss function has a clear disagreement with GT in reconstruction of individual real and imaginary components.

In order to check whether the observed reconstruction quality, demonstrated in Figures 9 and 10, is similar across all elements of the test sub-dataset, boxplots of the metric scores for each pair of model prediction and GT ($\hat{y}^{(i)}, x^{(i)}$) were generated.

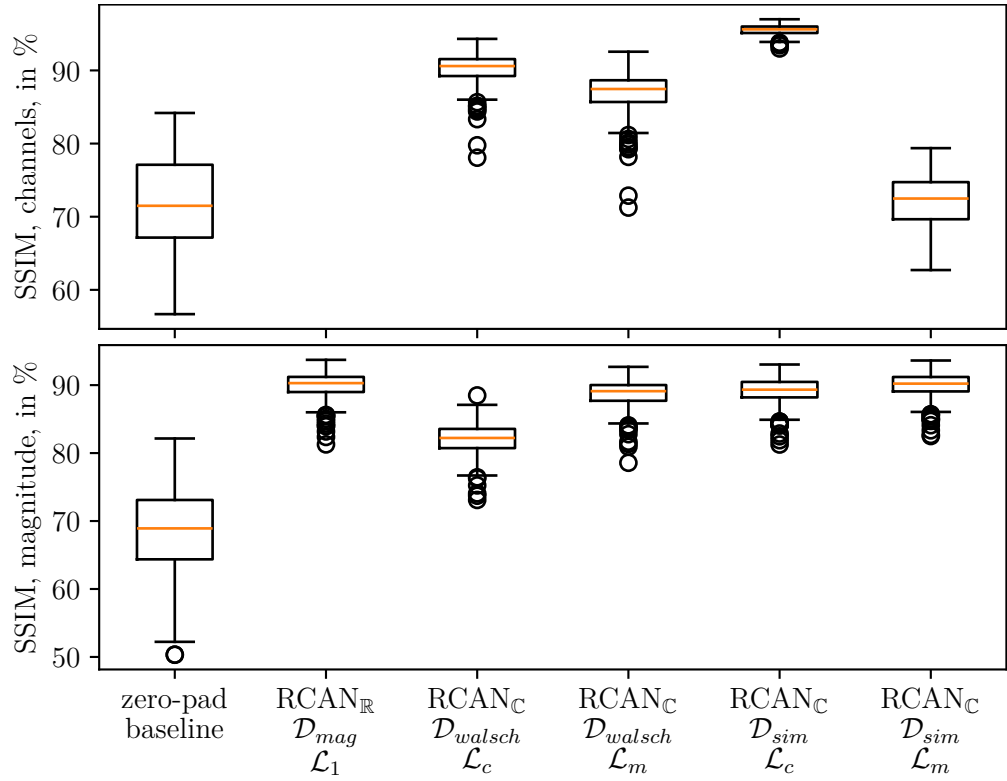


Figure 11: SSIM metric for (top) channels and (bottom) applied on test sub-dataset elements of each of DL model. Higher scores are better scores.

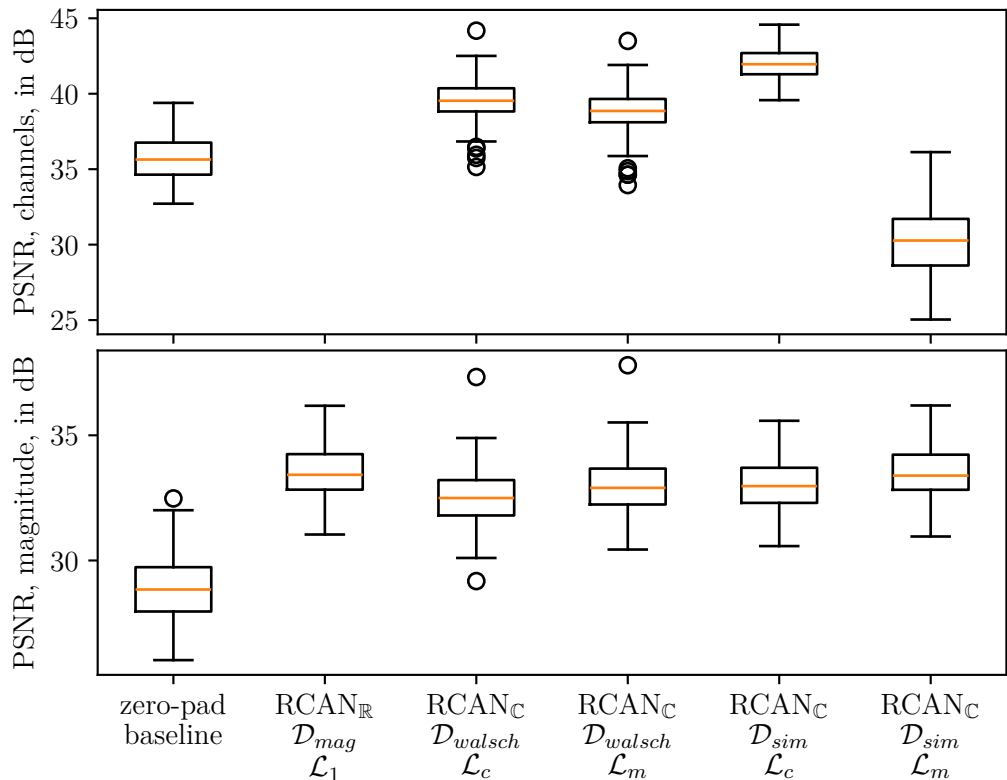


Figure 12: PSNR metric for (top) channels and (bottom) applied on test sub-dataset elements of each of DL model. Higher scores are better scores.

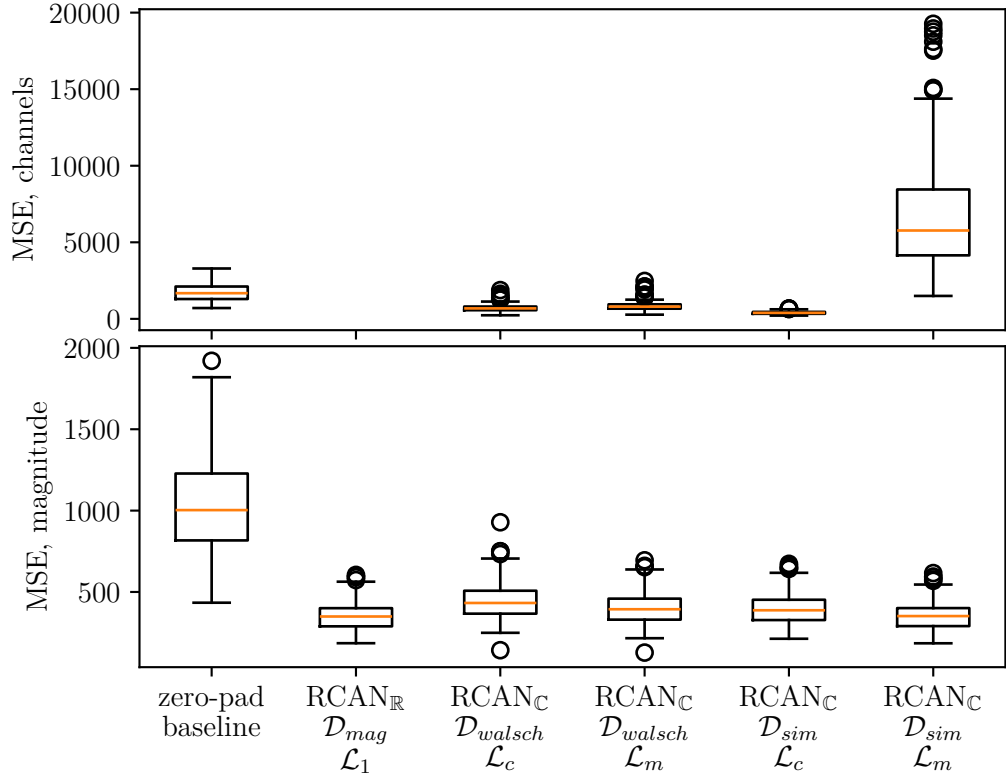


Figure 13: PSNR metric for (top) channels and (bottom) applied on test sub-dataset elements of each of DL model. Lower scores are better scores.

In Figures 11, 12 and 13 similar performance results, previously seen in Figures 9 and 10, are observed. While the $\text{RCAN}_{\mathbb{C}}$ model trained on the \mathcal{D}_{sim} with loss function \mathcal{L}_m achieves high metric scores for the resulting magnitude images, the model is not able to maintain high quality scores for individual channels. This is especially strong indicated by MSE metric in Figure 13.

Considering the median value of metrics scores and the width of Q1 and Q3 quantiles, the model $\text{RCAN}_{\mathbb{C}}$ trained on the \mathcal{D}_{sim} with loss function \mathcal{L}_m is capable to be used for denoising and super-resolution. However, the model is outperformed by the magnitude model $\text{RCAN}_{\mathbb{R}}$ in the magnitude reconstruction problem by approx. 1.5 % in the median scores for SSIM and PSNR metrics, with the largest performance observed in MSE metric at 11.2 %.

3.5 Discussion

In this Chapter, the DL model RCAN-like architecture, originally proposed for reconstruction of magnitudes images [24], was proven capable to be adapted for the reconstruction of complex-valued data represented as two channels and deliver feasible solutions for denoising and super-resolution problems.

Moreover, strong dependence of the DL model performance on the loss function, as well as the input data was observed. While the complex-valued DL model $\text{RCAN}_{\mathbb{C}}$ trained with \mathcal{L}_c loss function on the dataset of complex-valued data with simulated phase component was able to reconstruct both individual channels and magnitudes of the image, the same model configuration introduced hole-like artifacts, when was trained on the dataset of complex-valued data reconstructed with Walsh algorithm CSMs.

Across of the 4 different proposed complex-valued model configurations, only single model configuration, namely the model trained on the \mathcal{D}_{sim} with loss-function \mathcal{L}_c , was able to simultaneously produce consistent results and high image quality metrics scores for both individual channel and magnitudes.

Nevertheless, the complex-valued model did not outperform the magnitude model in the magnitude reconstruction task. Superior performance of the magnitude model can be attributed to use of the loss function \mathcal{L}_1 , which explicitly sets the training objective to minimise the magnitude difference. While the loss function \mathcal{L}_c , used for the complex-valued model, prioritises minimisation of the difference of individual channels.

	zero-pad baseline	RCAN _R	RCAN _C
median SSIM, magnitude, in %	68.92	90.29	89.33
median PSNR, magnitude, in dB	28.84	33.42	32.97
median MSE, magnitude	1003	349	388

Table 3.1: Better results for each metric are bold.

Although the magnitude based model RCAN_R slightly outperformed the complex-valued model RCAN_C in scores for SSIM and PSNR, the differences amount to approx. 1.5 %, with the largest difference in the MSE metric, where the RCAN_R model has an advantage of approx. 11.2 %.

4 Physics-informed reconstruction model

4.1 Introduction

In the previous Chapter, the complex-valued Deep-Learning (DL) model and the complex-valued dataset were prepared. The complex-valued DL model of Residual Channel Attention Network (RCAN) architecture has proven its capability for the denoising and super-resolution tasks, achieving high scores across performance metrics for individual complex imaginary and real components as well as for resulting magnitude images. Although the conventional magnitudes based model slightly outperformed the complex-valued model in metrics scores, the differences of Structural Similarity Index Measure (SSIM) and Peak Signal-to-Noise Ratio (PSNR) median values were below than 1.5 %, with the largest difference in the median score of Mean-Squared Error (MSE) metric, where the magnitude model has an advantage of approximately 11.2 %.

DL reconstruction models, however, can struggle with input data, which lays outside of the training data domain [52]. This is a particularly relevant for the case of application of the DL model on a real-world Ultra-Low-Field (ULF) Magnetic Resonance Imaging (MRI) acquisition, while the DL model was trained on simulated data.

By incorporating knowledge of the MRI acquisition model into the reconstruction model, the Physics-Informed Neural Network (PINN) can become increase consistency level with the input and deliver better reconstruction quality compared to the reconstruction made by the individual results of DL model or classical reconstruction model [53–56].

In the following Chapter, previously developed complex-valued $\text{RCAN}_{\mathbb{C}}$ model is extended with the underlying physics model of MRI acquisition process. Two distinct approaches of physics-informed reconstruction are proposed. In first approach, predictions of DL model are used as a regularisation term in the inverse reconstruction problem. The second approach employs an End-to-End (E2E) training procedure, in which the model training objective is explicitly set to solve the physically-informed inverse reconstruction problem. Then, performance of the physics-informed model is evaluated and compared with that of the purely DL models, previously developed in Chapter 3.

In addition, the performance of the physics-informed and purely DL models is evaluated in the context of accelerated measurements, where the model inputs correspond to in k -space undersampled data. Different strategies for sampling of k -space are examined and performance of models for different degrees of k -space sampling are evaluated.

4.2 Methods

4.2.1 Regularisation problem for the acquisition model operator

With general Equation 2.22 we now define the acquisition operator \mathbf{A} as follows

$$\mathbf{A} : \mathbb{C}^{z \times y \times x} \rightarrow \mathbb{C}^{z_l \times y_l \times x_l} = \mathbf{D}\mathbf{F}, \quad (4.1)$$

with $\mathbf{F} : \mathbb{C}^{z \times y \times x} \rightarrow \mathbb{C}^{z \times y \times x}$ being Fast Fourier Transform (FFT) operator and $\mathbf{D} : \mathbb{C}^{z \times y \times x} \rightarrow \mathbb{C}^{z_l \times y_l \times x_l}$ being a sampling operator matching the k -space data over the same k -space sampling trajectory as \mathbf{m}^k .

Now, Equation 2.26 can be reformulated using prediction of the deep-learning model \mathbf{u}_r for measured input \mathbf{m}^k as the regularisation term $\mathcal{R}(\mathbf{u})$:

$$\mathbf{u}_0 = \arg \min_{\mathbf{u}} \left\{ \frac{1}{2} \left\| \mathbf{A}\mathbf{u} - \mathbf{m}^k \right\|_2^2 + \frac{\lambda}{2} \left\| \mathbf{u} - \mathbf{u}_r \right\|_2^2 \right\} \quad (4.2)$$

The formal solution for \mathbf{u} derived in Equation 2.29 yields

$$(\mathbf{A}^H \mathbf{A} + \lambda \mathbf{I})\mathbf{u} = \mathbf{A}^H \mathbf{m}^k + \lambda \mathbf{u}_r \quad (4.3)$$

The equivalent representation of the sampling operator \mathbf{D} is the element-wise product (*Hadamard product*) with a tensor \mathbf{M}_{ijk} of zeros and ones, being a binary mask for the values on the three-dimensional Cartesian grid in the k -space. The tensor entries take the value one for sampled data points and zero for non-sampled points of measurement \mathbf{m}^k . The operator \mathbf{D} is self-adjoint

$$\mathbf{D} = \mathbf{D}^H \quad (4.4)$$

and, since the tensor elements \mathbf{M}_{ijk} are only zeros and ones, is idempotent, more precisely:

$$\mathbf{D}^n \mathbf{a} = (\mathbf{M}_{ijk})^n \mathbf{a}_{ijk} \stackrel{M_{ijk} \in \{0,1\}}{=} \mathbf{M}_{ijk} \mathbf{a}_{ijk} = \mathbf{D}\mathbf{a}, \forall n \in \mathbb{N} \quad (4.5)$$

With the acquisition operator $\mathbf{A} = \mathbf{D}\mathbf{F}$, the formal solution for \mathbf{u} in Equation 4.3 is equivalent to

$$((\mathbf{D}\mathbf{F})^H \mathbf{D}\mathbf{F} + \lambda \mathbf{I})\mathbf{u} = (\mathbf{D}\mathbf{F})^H \mathbf{m}^k + \lambda \mathbf{u}_r, \quad (4.6)$$

and has a closed-form solution. With the properties of the operator \mathbf{D} proven earlier, the left- and right-hand sides of Equation 4.6 are equivalent to

$$\begin{cases} (\mathbf{F}^H \mathbf{D}^H \mathbf{D}\mathbf{F} + \lambda \mathbf{I})\mathbf{u} & \stackrel{(4.4)}{=} (\mathbf{F}^H \mathbf{D}^2 \mathbf{F} + \lambda \mathbf{I})\mathbf{u} \stackrel{(4.5)}{=} (\mathbf{F}^H \mathbf{D}\mathbf{F} + \lambda \mathbf{I})\mathbf{u} \\ \mathbf{F}^H \mathbf{D}^H \mathbf{m}^k + \lambda \mathbf{u}_r & \stackrel{(4.4)}{=} \mathbf{F}^H \mathbf{D}\mathbf{m}^k + \lambda \mathbf{u}_r \end{cases} \quad (4.7)$$

yielding the following Equation:

$$(\mathbf{F}^H \mathbf{D}\mathbf{F} + \lambda \mathbf{I})\mathbf{u} = \mathbf{F}^H \mathbf{D}\mathbf{m}^k + \lambda \mathbf{u}_r \quad (4.8)$$

Applying the operator \mathbf{F} from the left to both sides of Equation 4.8, the following expression in

k -space is derived, where $\mathbf{u}^k = \mathbf{F}\mathbf{u}$ and $\mathbf{u}_r^k = \mathbf{F}\mathbf{u}_r$. Since the operator \mathbf{F} is unitary ($\mathbf{F}\mathbf{F}^H = \mathbf{I}$):

$$\mathbf{D}\mathbf{u}^k + \lambda\mathbf{I}\mathbf{u}^k = \mathbf{D}\mathbf{m}^k + \lambda\mathbf{u}_r^k \quad (4.9)$$

Substitution of \mathbf{D} by the Hadamard product with the binary mask tensor \mathbf{M} yields:

$$\mathbf{M}_{ijk}\mathbf{u}_{ijk}^k + \lambda\mathbf{u}_{ijk}^k = \mathbf{M}_{ijk}\mathbf{m}_{ijk}^k + \lambda\mathbf{u}_{r,ijk}^k \quad (4.10)$$

and can be further split into two cases, depending on the value of the tensor entry \mathbf{M}_{ijk}

$$\begin{cases} \mathbf{u}_{ijk}^k + \lambda\mathbf{u}_{ijk}^k = \mathbf{m}_{ijk}^k + \lambda\mathbf{u}_{r,ijk}^k & \text{for } \mathbf{M}_{ijk} = 1 \\ \lambda\mathbf{u}_{ijk}^k = \lambda\mathbf{u}_{r,ijk}^k & \text{for } \mathbf{M}_{ijk} = 0 \end{cases} \quad (4.11)$$

resulting into two-cases solution for \mathbf{u}_{ijk}^k

$$\begin{cases} \mathbf{u}_{ijk}^k = \frac{\mathbf{m}_{ijk}^k + \lambda\mathbf{u}_{r,ijk}^k}{1 + \lambda} & \text{for } \mathbf{M}_{ijk} = 1 \\ \mathbf{u}_{ijk}^k = \mathbf{u}_{r,ijk}^k & \text{for } \mathbf{M}_{ijk} = 0 \end{cases} \quad (4.12)$$

with the final solution for the \mathbf{u}

$$\mathbf{u} = \mathbf{F}^H\mathbf{u}^k. \quad (4.13)$$

This can be intuitively understood as either taking only the model prediction value in k -space for non-sampled value, or taking a λ weighted average of the measured value \mathbf{m}_{ijk}^k and model prediction $\mathbf{u}_{r,ijk}^k$, and then apply the inverse Fourier transform operator \mathbf{F}^H .

Closed-form solution for \mathbf{u} , derived in Equations 4.12 and 4.13, can be implemented as a function:

Algorithm 3 Function $DC(x, \hat{y}, \lambda)$

Require: Measurement x , Model prediction \hat{y} , Regularisation weight $\lambda > 0$, Mask tensor $\mathbf{M}_{ijk} \in \{0, 1\}$

```

1: function DC( $x, \hat{y}, \lambda$ )
2:    $x^k \leftarrow \text{FFT}(x)$ 
3:    $\hat{y}^k \leftarrow \text{FFT}(\hat{y})$ 
4:   for all  $i, j, k$  do
5:      $u_{ijk}^k \leftarrow \frac{x_{ijk}^k + \lambda\hat{y}_{ijk}^k}{\mathbf{M}_{ijk} + \lambda}$ 
6:   end for
7:    $u \leftarrow \text{IFFT}(u^k)$ 
8:   return  $u$ 
9: end function

```

4.2.2 End-to-end training

Training scheme, used in Chapter 3, set the minimisation of difference between the DL model prediction and Ground Truth (GT). With E2E learning, the complete inverse reconstruction problem from Equation 4.2 is being set as the training objective for the DL model. This enforces the DL prediction to be consistent with the physical acquisition model of ULF MRI.

The E2E learning scheme is very similar to the supervised learning algorithm shown in Algo-

rithm 1, but has an additional intermediate *data-consistency* step based on the function DC from Algorithm 3:

Algorithm 4 End-to-End (E2E) supervised learning algorithm for an ANN

Require: Model M , Loss function \mathcal{L} , Training data $\mathcal{D} = \{(x^{(i)}, y^{(i)})\}_{i=1}^N$, Parameters state w , Batch size B , Learning rate η , Number of epochs E , Data-consistency function DC

- 1: **for** epoch = 1 to E **do**
- 2: **for** each training batch $\{(x^{(n)}, y^{(n)})\}_{n=1}^B \subset \mathcal{D}$ **do**
- 3: **Forward pass:** Compute predictions $\{\hat{y}^{(n)}\}_{n=1}^B := M(\{x^{(n)}\}_{n=1}^B; w)$
- 4: **Data consistency:** $\{\hat{y}'^{(n)} := DC(x^{(n)}, \hat{y}^{(n)}, \lambda)\}_{n=1}^B$
- 5: **Compute loss:** $L := \sum_n^B \mathcal{L}(\hat{y}'^{(n)}, y^{(n)})$
- 6: **Backward pass:** Compute gradients $\nabla_w L$
- 7: **Update parameters:** $w \leftarrow w - \eta \cdot \nabla_w L$
- 8: **end for**
- 9: **end for**

The algorithm for prediction of E2E trained model slightly differs from one for the simple supervised learning (Algorithm 2), as it includes an additional data-consistency step using the same function DC , used during E2E training:

Algorithm 5 End-to-End (E2E) supervised learned model prediction

Require: Model M , Parameters state w , Regularisation data-consistency function DC

- 1: **Input:** $x^{(i)}$
- 2: **Predict:** $\hat{y}^{(i)} := M(x^{(i)}; w)$
- 3: **Data consistency:** $\hat{y}'^{(i)} := DC(x^{(i)}, \hat{y}^{(i)}, \lambda)$
- 4: **return** $\hat{y}'^{(i)}$

With an assumption that the DL model prediction for the physics-informed reconstruction problem is similar to the prediction without data-consistency term, the parameters state w of the DL model M , trained without data-consistency step, can be used as an initial state for the E2E. This technique is widely used in DL model training to reduce the duration of training and known as *transfer learning*.

4.3 Experiments

The complex-valued DL model RCAN_C configuration with loss function \mathcal{L}_c , earlier proposed in Chapter 3, is used for the experiments. All trainings are performed on the train sub-dataset of the \mathcal{D}_{sim} dataset. Optimisation parameters, such as learning rate, batch size and optimiser, remain unchanged to those used in Chapter 3.

The state of DL model parameter w , trained with supervised learning (Algorithm 1) for 120 epochs, is used as the initial state of the DL model trained for additional 60 epochs of E2E training (Algorithm 4).

4.3.1 Super-resolution and denoising problem

Firstly, the closed-form solutions for reconstruction problem, derived in Algorithm 3, for the simulated measurements $x^{(i)}$ of test sub-dataset of \mathcal{D}_{sim} with corresponding RCAN_C model predictions $\hat{y}^{(i)}$ are evaluated for different values of regularisation weight $\lambda \in \{1 \times 10^{-3}, 1 \times 10^{-2}, 0.1, 0.3, 0.6, 1.0, 2.0, 10\}$. Goal of this particular experiment is to determine whether there exists a regularisation weight λ that yields a solution with a higher performance score than either the reconstruction without regularisation term or the DL model prediction alone. Furthermore, if such a regularisation weight exists, the experiment aims to identify the value of λ that maximises the performance of the joint solution. For the performance evaluation of the solution the same SSIM, PSNR and MSE metrics were applied, as in Chapter 3. Then, the E2E training is performed with the fixed value of regularisation weight λ .

In order to differentiate, whether change in model performance originates from the E2E training scheme or simply because of the additional training epochs, the reference DL models with the same initial parameter state w are trained with a general supervised learning scheme (Algorithm 1) for the same number of additional training epochs.

4.3.2 Super-resolution, denoising and undersampling problem

The DL models were trained on the partially sampled input data $x^{(i)}$ with the k -space sampling degree of 80 %, 60 % and 55 % with the Partial Fourier (PF) and Gaussian Sampling (GS) patterns. For the three-dimensional Cartesian k -space these patterns can be represented as binary masks in form of three-dimensional tensor with values of ones and zeros. The x - y slices of binary masks tensors \mathbf{M}_{ijk} are shown in Figure 14. The slices along the z -axis are identical

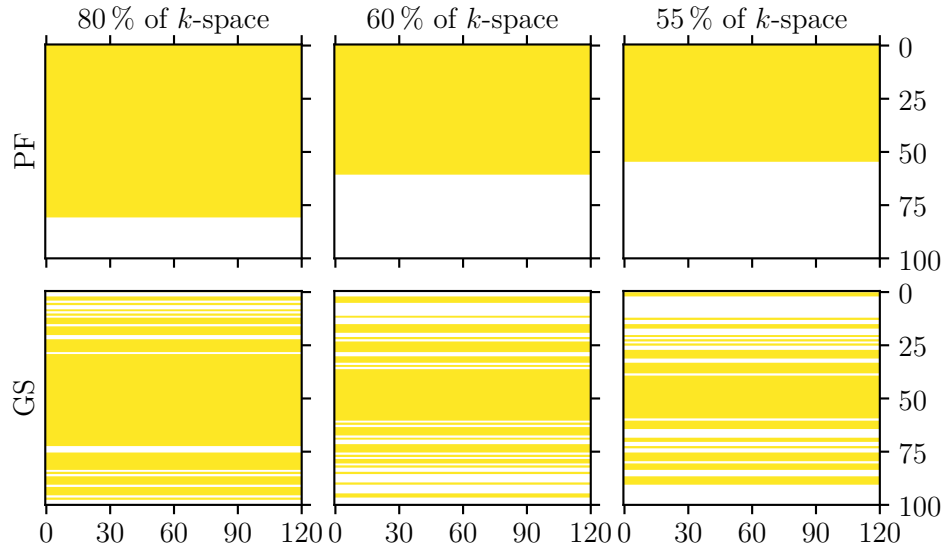


Figure 14: Slices of tensors \mathbf{M}_{ijk} represented in the k -space for Partial Fourier (PF) and Gaussian Sampling (GS). Shown are the x - y slices which are identical for each of the slices along the z -axis. Yellow corresponds to value of one and white corresponds to zero. The outer region of masks is padded with zeros to the shape of $200 \times 240 \text{ px}^2$.

Then, the output data $\hat{y}^{(i)}$ of the test sub-dataset was regularised with the same set of weights λ as written above to find if any intermediate value of the range would perform better for the solution

than the output of the $\text{RCAN}_{\mathbb{C}}$ model alone.

In total, 12 models were trained by evaluating every possible combination of the two model variants $\{\text{RCAN}_{\mathbb{C}}, \text{RCAN}_{\mathbb{R}}\}$, the two sampling patterns $\{\text{PF}, \text{GS}\}$, and three sampling degrees $\{80\%, 60\% \text{ and } 55\%\}$. These models were trained for 120 epochs.

Then, 6 models $\text{RCAN}_{\mathbb{C}}$ were trained E2E for 60 more epochs with a fixed regularisation weight λ . And finally, the 6 reference $\text{RCAN}_{\mathbb{C}}$ and 6 reference $\text{RCAN}_{\mathbb{R}}$ models without E2E were trained 60 more epochs to get reference models with the same final number of training epochs of 180.

4.4 Results

4.4.1 Super-resolution and denoising problem

The solutions \mathbf{u} for the reconstruction problem (Equation 4.2) were evaluated with the Algorithm 3 with a set of different values of λ and predictions of the model $\text{RCAN}_{\mathbb{C}}$. Those are exemplarily shown in Figure 15.

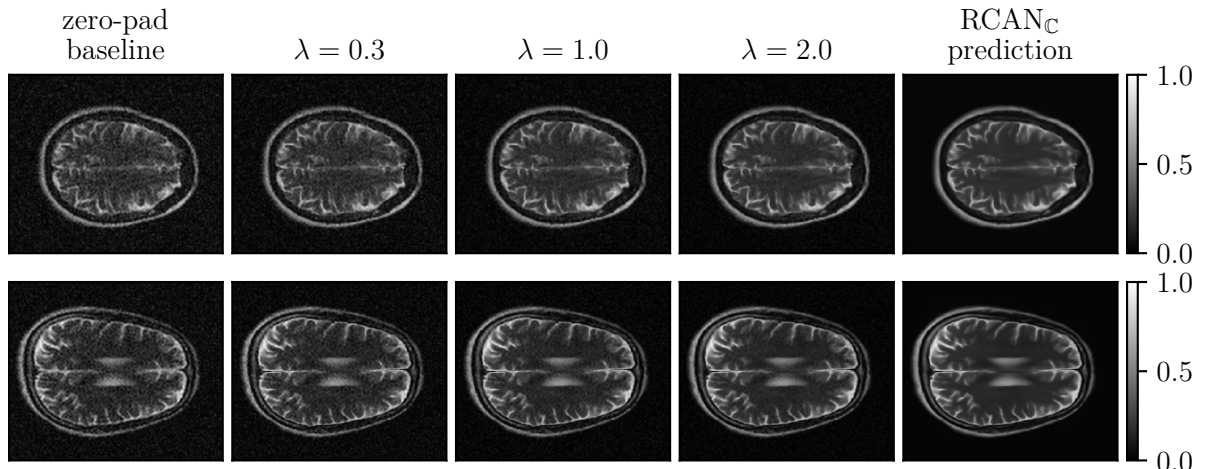


Figure 15: Magnitudes of "zero-pad" baseline reconstructions, as well as the solutions for the reconstruction problem \mathbf{u} for intermediate values of λ are evaluated. With increase of the value λ the noise level reduces and image appearance becomes more similar to the prediction of the $\text{RCAN}_{\mathbb{C}}$ model.

Then the quality performance metrics of the solutions $\hat{y}^{(i)}$ and GT $y^{(i)}$ were evaluated. For the analysis of the reconstruction performance, boxplot of SSIM metric is generated and shown in Figure 16.

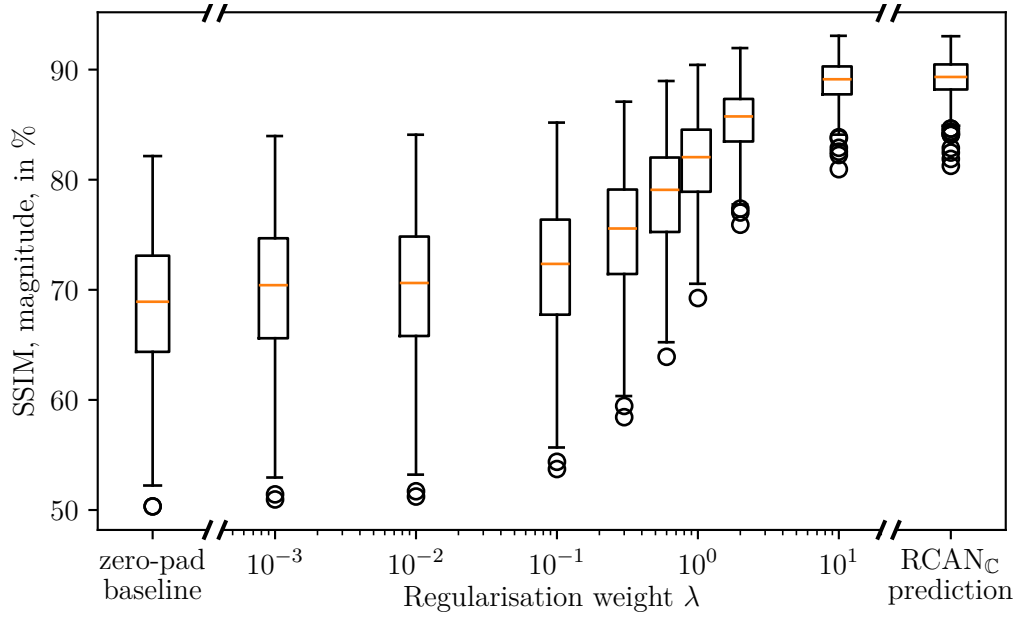


Figure 16: SSIM for the fully sampled input RCAN_C with the regularisation with different weights λ . Values of the edge cases of very small lambda and greater lambda asymptotically approach the (left) zero-pad baseline reconstruction performance and (right) predictions of the DL model alone.

Since the performance metric scores continuously grow with the increase of regularisation weight λ , the regularisation weight $\lambda = 1$, which equalises the contribution of the measurement $x^{(i)}$ and the DL model prediction $\hat{y}^{(i)}$ to the final result \mathbf{u} , was chosen for E2E supervised training. Change of loss function over the training epoch during the training, shown in Figure 17, indicates an increase of loss function in case of E2E learning, which does not decline faster than the reference model with continued training.

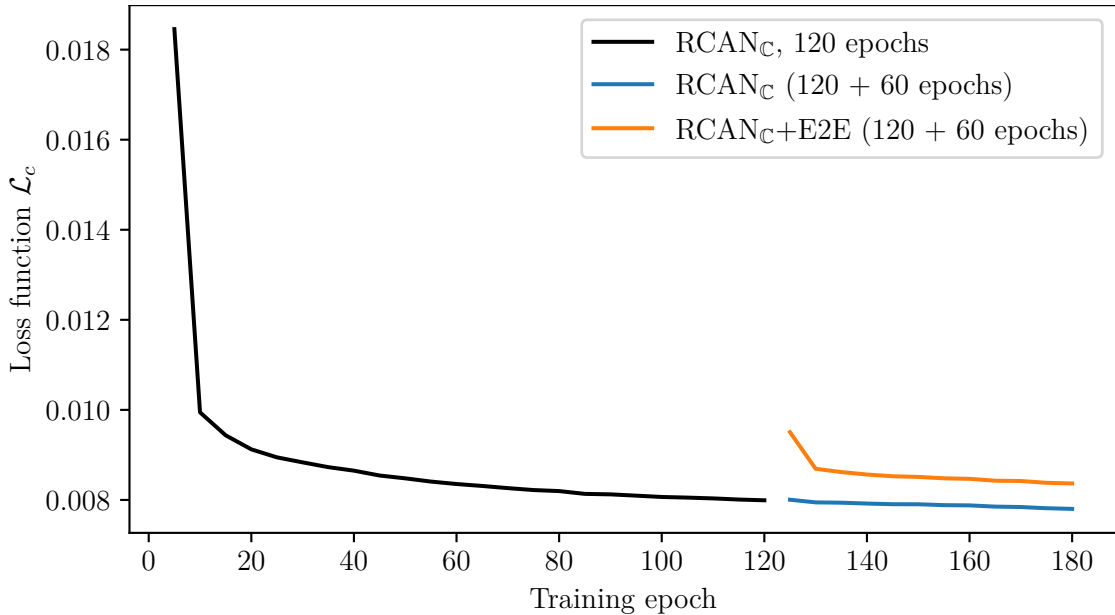


Figure 17: Change of loss function \mathcal{L}_c value throughout the training. The first loss function value of each training session was unintentionally not recorded.

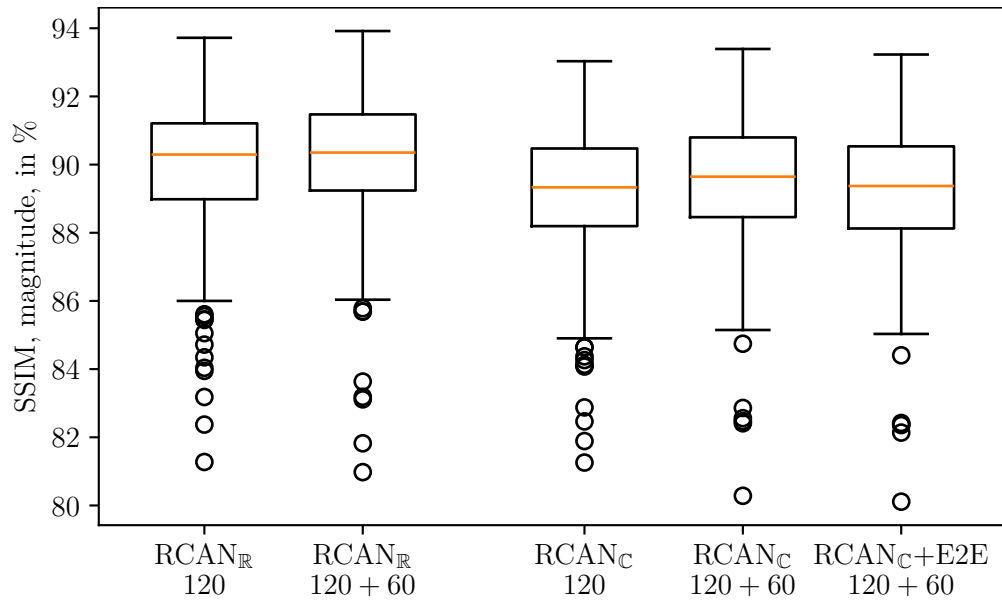


Figure 18: SSIM metrics scores for the magnitude models $\text{RCAN}_{\mathbb{R}}$ trained with supervised learning of 120 and $(120 + 60)$ epochs. And the complex-valued model $\text{RCAN}_{\mathbb{C}}$ trained for 120 epochs, as well as model with E2E training and reference model with $(120 + 60)$ epochs of training.

In Figure 18 the results of SSIM for the model of $\text{RCAN}_{\mathbb{C}}$ trained with the 120 epochs of supervised learning (shown in Chapter 3), the $\text{RCAN}_{\mathbb{C}}$ model with additional 60 epochs of supervised learning and the $\text{RCAN}_{\mathbb{C}}+\text{E2E}$ model trained for additional 60 epochs of E2E supervised learning are shown.

The $\text{RCAN}_{\mathbb{C}}+\text{E2E}$ model trained for 60 more epochs performed better than the $\text{RCAN}_{\mathbb{C}}$ model trained for 120 epochs. However, it was outperformed by the model $\text{RCAN}_{\mathbb{C}}$ trained for 60 more epochs without the E2E training scheme.

4.4.2 Super-resolution, denoising and undersampling problem

Partial Fourier sampling

The $\text{RCAN}_{\mathbb{C}}$ and $\text{RCAN}_{\mathbb{R}}$ models were trained on the partially sampled inputs $x^{(i)}$. The inputs are sampled with the Partial Fourier (PF) sampling of 80 %, 60 % and 55 %. The predictions of the $\text{RCAN}_{\mathbb{C}}$ models are shown exemplarily in Figure 19.

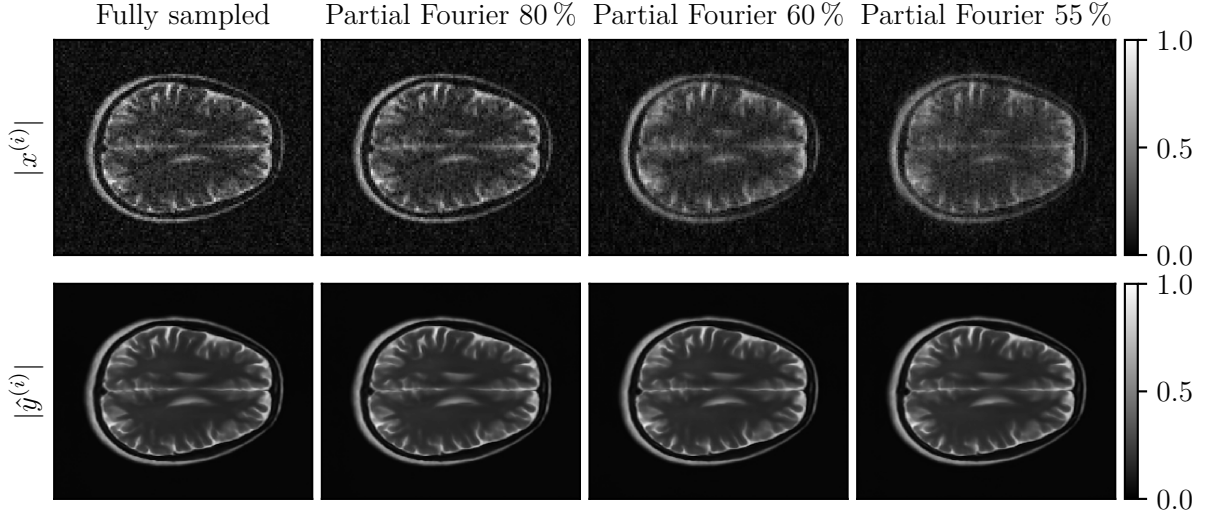


Figure 19: Magnitude of input $|x^{(i)}|$ (top row) of the fully sampled, undersampling with the PF of 80%, 60% and 55% and magnitudes of the RCAN_C models $|\hat{y}^{(i)}|$.

In Figure 20 are SSIM scores for the RCAN_C models predictions with GT for various sampling degrees are shown.

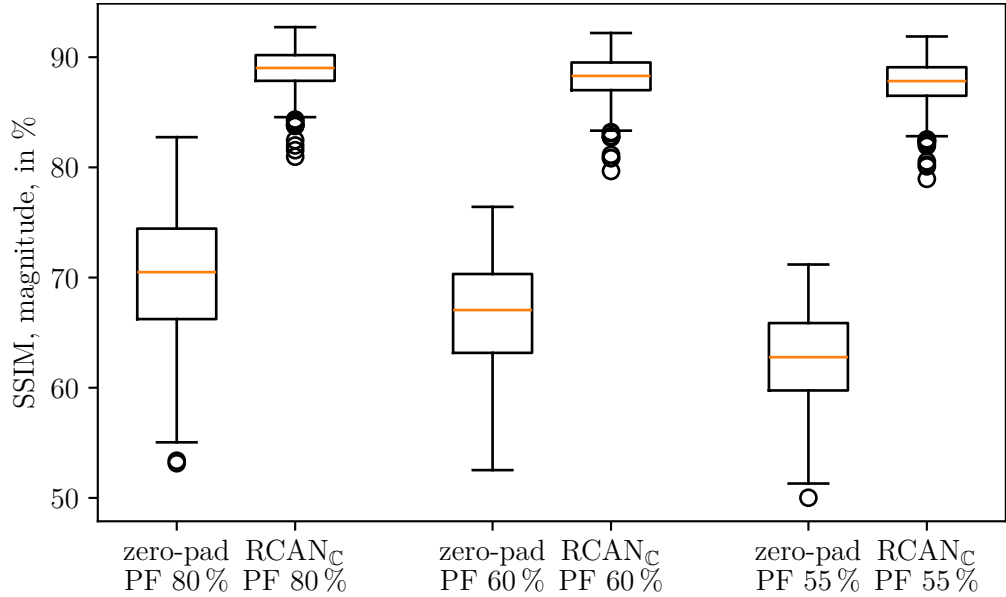


Figure 20: SSIM for magnitudes metrics of the RCAN_C prediction for the different degrees of PF sampling trained for 120 epochs of supervised learning.

This shows the ability of RCAN_C models to also improve the reconstruction quality in case of partial PF sampling.

Then, the search for an optimal λ , which would improve the performance metrics results, was done for each model of each sampling degree, in the same way as in Subsection 4.3.1.

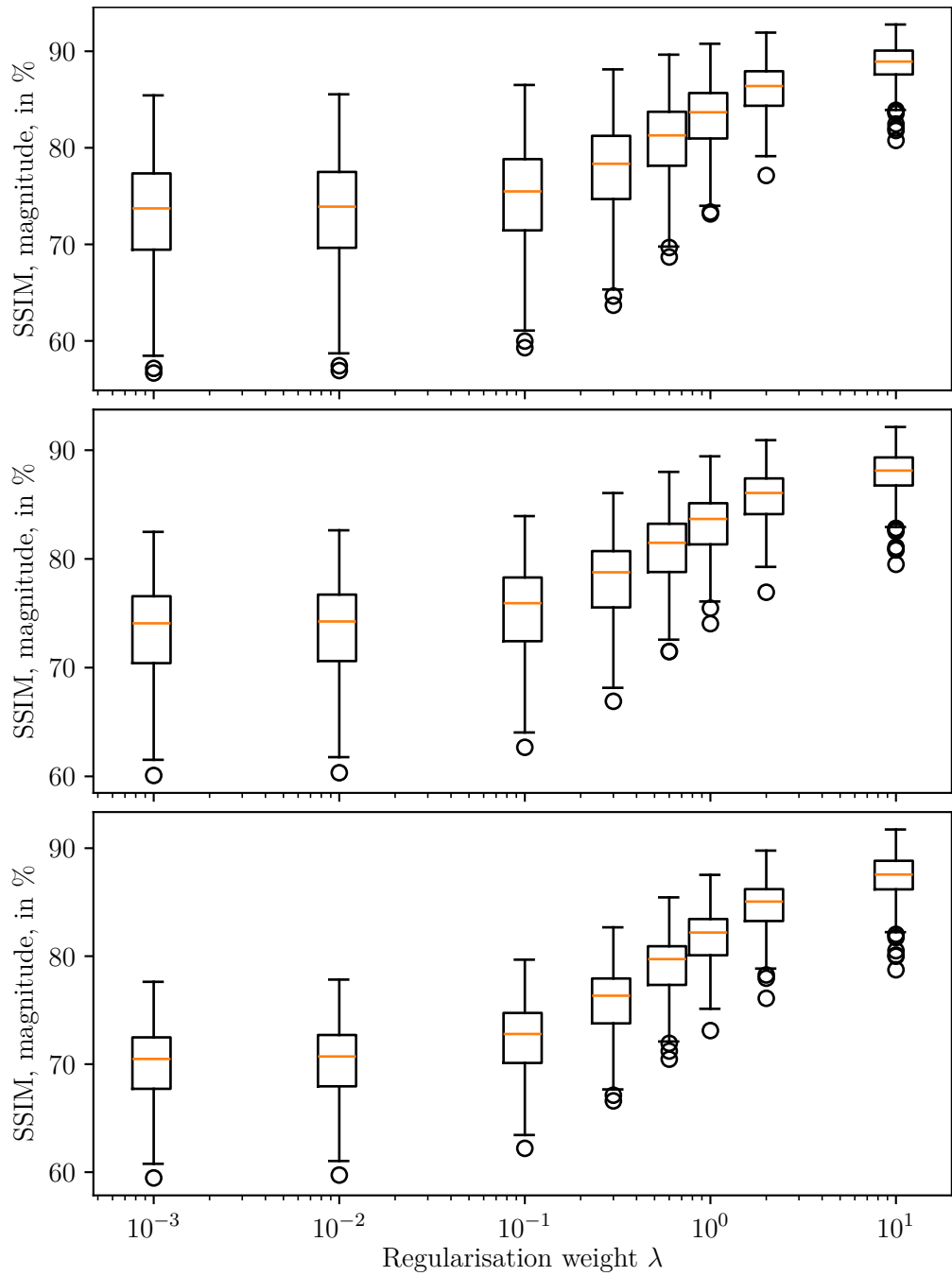


Figure 21: SSIM of regularised predictions RCAN_C for PF sampling degrees of (top) 80 %, (middle) 60 % and (bottom) 55 %.

In Figure 21 the same behaviour for the PF sampled data, as for the fully sampled data is observed. There is a straight tendency with increase of performance metrics with increasing regularisation weight λ for each of the PF sampling degrees. Therefore, the E2E trained models were trained with the constant regularisation weight $\lambda = 1$.

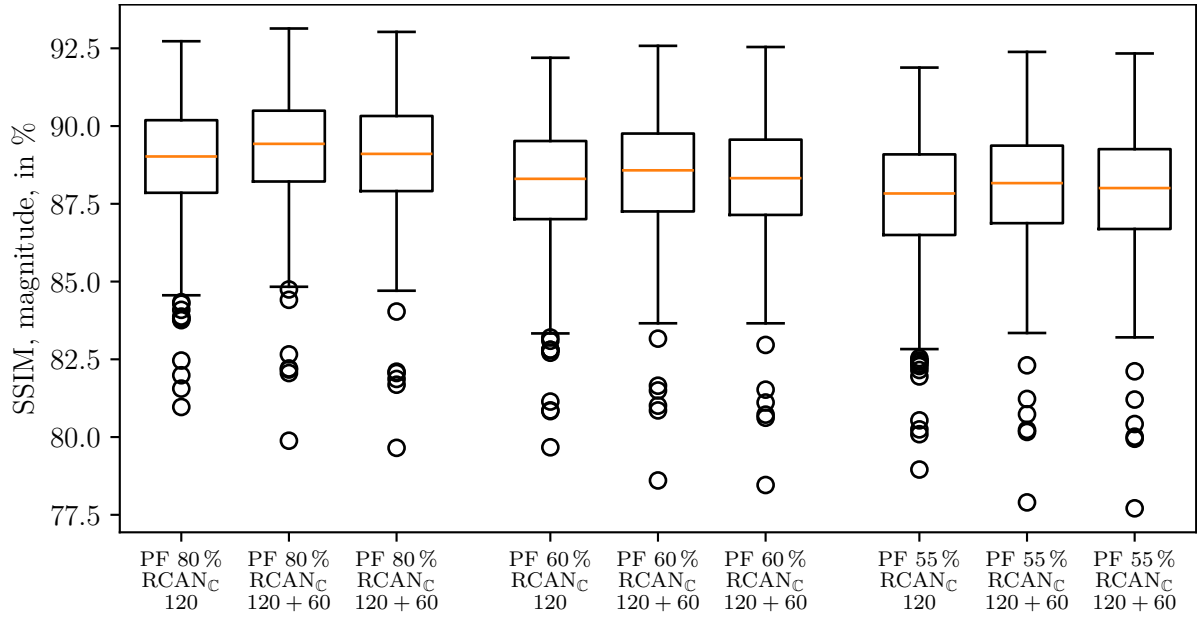


Figure 22: For each of PF sampling degrees three models are evaluated. The RCAN_C (left) trained with supervised learning with 120 epochs, the RCAN_C (middle) with additional 60 epochs of supervised learning, and (right) RCAN_C+E2E with additional 60 epochs of E2E supervised learning. The groups of box-plots, from left to right, correspond to 80 %, 60 % and 55 % of PF sampling degrees.

In Figure 22 SSIM results for PF sampling of different sampling degrees are shown. For each of the PF sampling degree of 80 %, 60 % and 55 %, the RCAN_C trained with additional 60 epochs of supervised learning demonstrated the best performance metrics results, compared to the RCAN_C+E2E trained with additional 60 epochs of E2E learning.

Gaussian random sampling

The RCAN_C and RCAN_R models were trained and the outputs of the models with the different GS degrees of 80 %, 60 % and 55 %, with sampling masks shown in Figure 14. The predictions of the RCAN_C models are shown exemplarily in Figure 23.

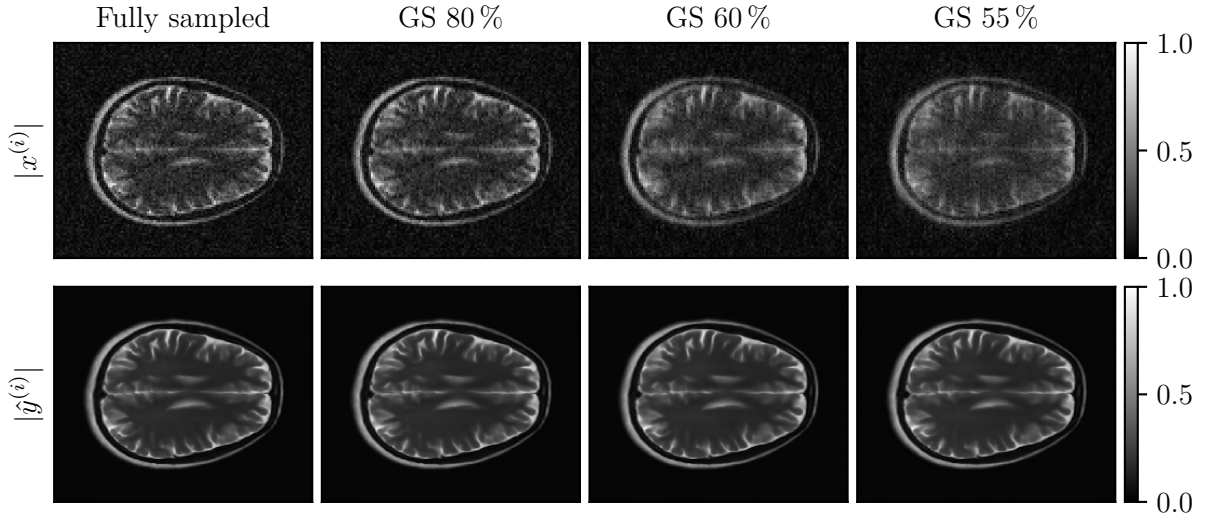


Figure 23: Magnitudes of (top row) input $|x^{(i)}|$ of the fully sampled, partially sampled by 80 %, 60 % and 55 % with the GS and magnitudes of (bottom row) the RCAN_C models $|\hat{y}^{(i)}|$.

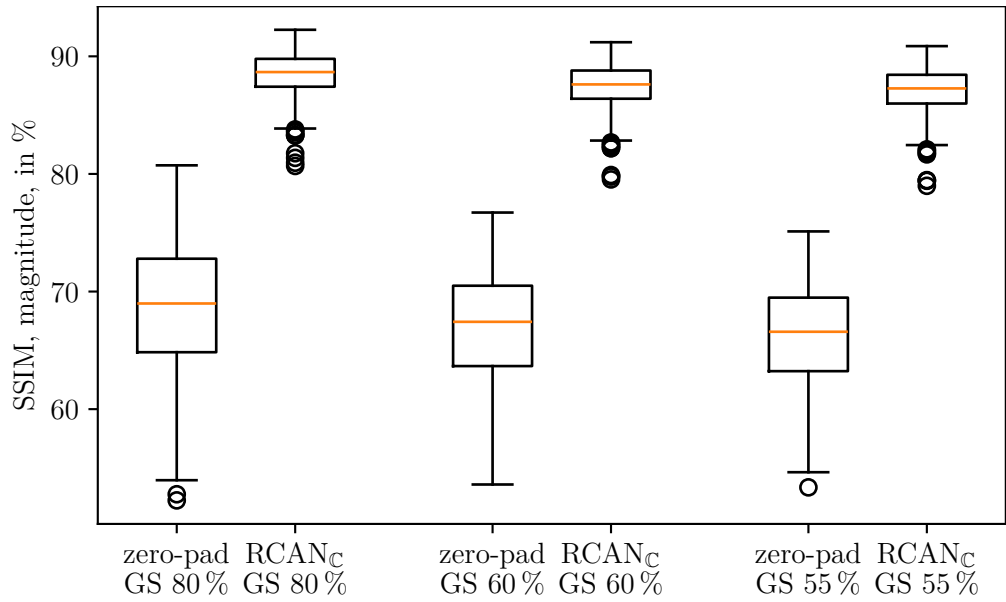


Figure 24: SSIM for magnitudes metrics of the RCAN_C prediction for the different degrees of GS trained for 120 epochs of supervised learning.

Then, the search of an optimal λ , improving the performance metrics results, was done for each model of each undersampling degree, in the same way as done for PF sampling.

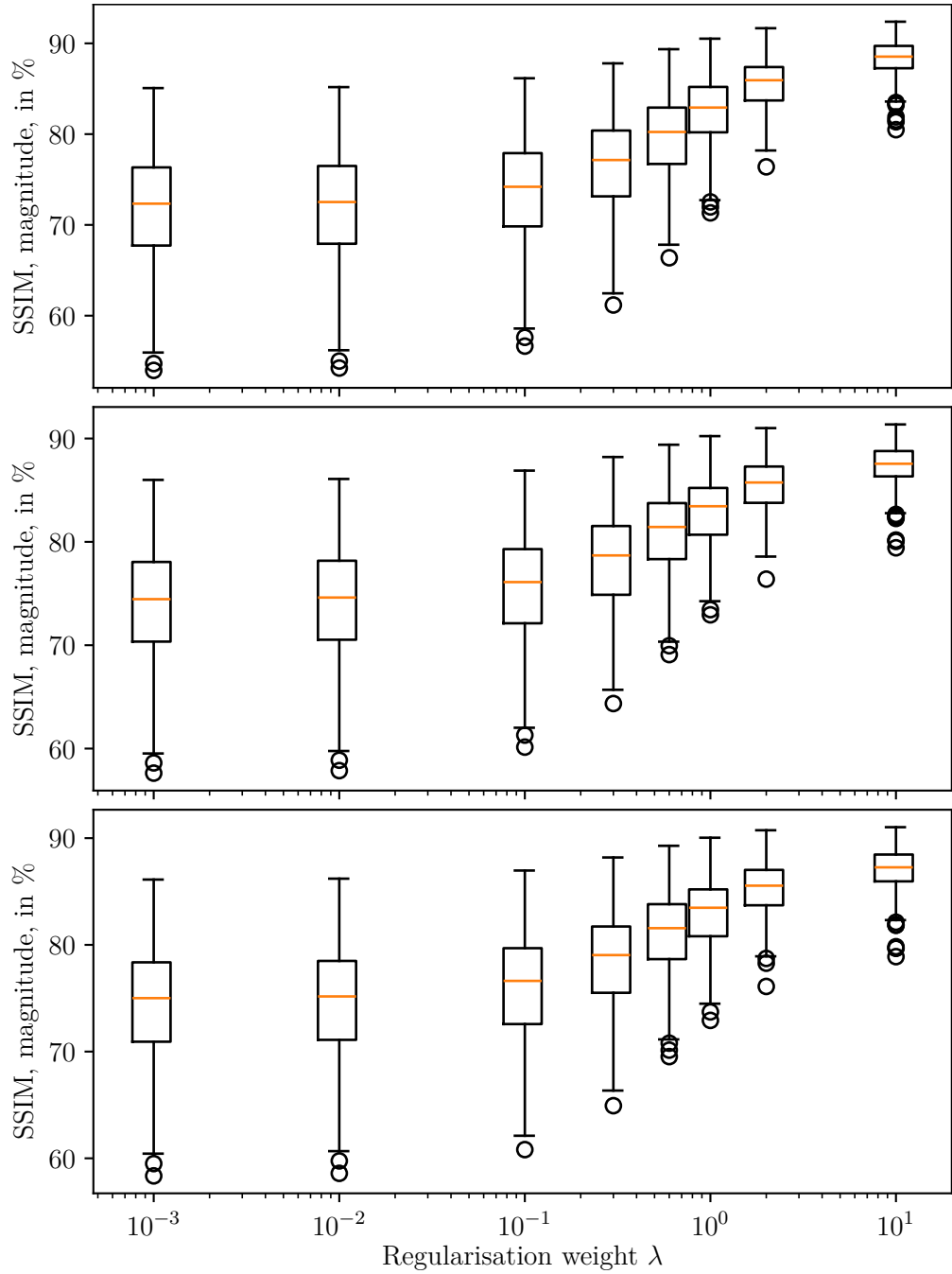


Figure 25: SSIM of regularised predictions RCAN_c for GS degrees of (top) 80 %, (middle) 60 % and (bottom) 55 %.

For the GS partially sampled data the same behaviour of the metrics for regularisation in respect to λ is observed. The performance metrics are increasing with increasing value of regularisation weight λ for all sampling degrees. Therefore, for the E2E the constant regularisation weight $\lambda = 1$ is selected, which equalises contributions of the measurement \mathbf{m}^k and the model prediction \mathbf{u}_r .

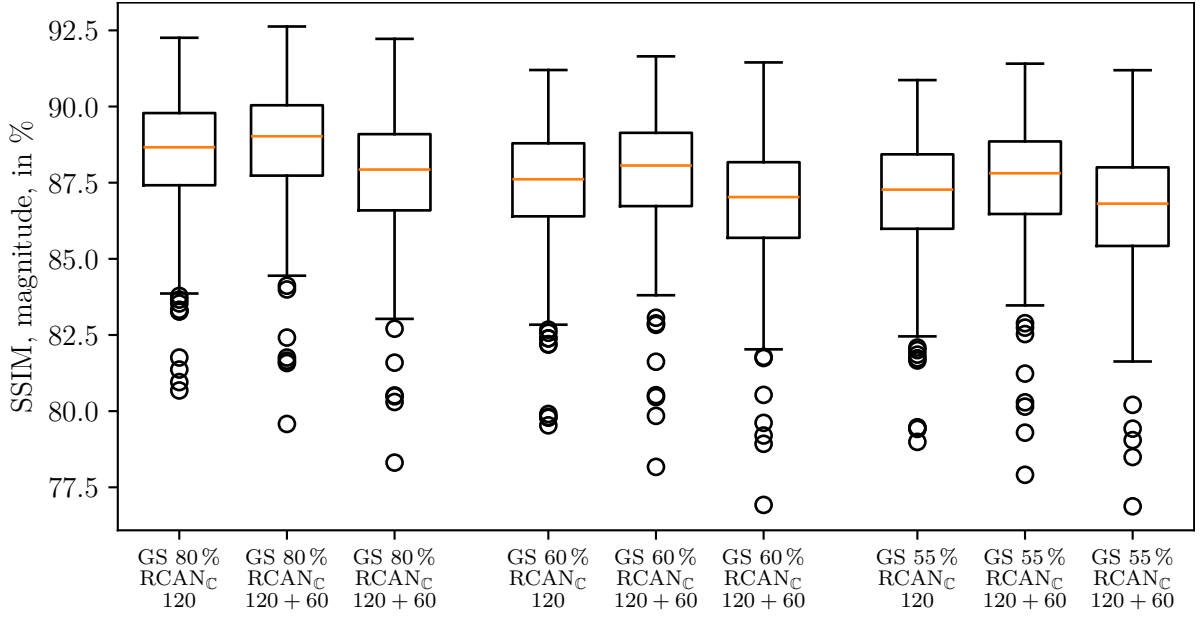


Figure 26: For each of GS degrees three models are evaluated. The $\text{RCAN}_{\mathbb{C}}$ (left) trained with supervised learning with 120 epochs, the $\text{RCAN}_{\mathbb{C}}$ (middle) with additional 60 epochs of supervised learning, and (right) $\text{RCAN}_{\mathbb{C}}+\text{E2E}$ with additional 60 epochs of E2E supervised learning. The groups of boxplots, from left to right, correspond to 80 %, 60 % and 55 % of GS degrees.

In Figure 26 SSIM results for GS of different sampling degrees are shown. For each of the GS degree of 80 %, 60 % and 55 %, the $\text{RCAN}_{\mathbb{C}}$ trained with additional 60 epochs of supervised learning demonstrated the best performance metrics scores, compared to the $\text{RCAN}_{\mathbb{C}}+\text{E2E}$ trained with additional 60 epochs with E2E. In contrary with the fully sampled and PF undersampling acquisitions, the $\text{RCAN}_{\mathbb{C}}+\text{E2E}$ model performance degraded in comparison with the prediction of model $\text{RCAN}_{\mathbb{C}}$.

4.5 Discussion

4.5.1 Super-resolution and denoising problem

The dependence on SSIM on the regularisation weight λ , shown in Figure 16, indicates a monotonic increase of SSIM value proportional to the value of λ . Indeed, with increase of λ metric scores are increasing and approaching the score of the $\text{RCAN}_{\mathbb{C}}$ model. For the smallest value $\lambda = 1 \times 10^{-3}$ the SSIM metric score converges towards the those of the "zero-pad baseline" reconstruction. These extreme cases of large and small regularisation weight λ are consistent with Equation 4.12, which yields

$$\begin{aligned} \lim_{\lambda \rightarrow 0} \frac{\mathbf{m}_{ijk}^k + \lambda \mathbf{u}_{r,ijk}^k}{1 + \lambda} &= \mathbf{m}_{ijk}^k \\ \lim_{\lambda \rightarrow \infty} \frac{\mathbf{m}_{ijk}^k + \lambda \mathbf{u}_{r,ijk}^k}{1 + \lambda} &= \mathbf{u}_{r,ijk}^k \end{aligned} \quad (4.14)$$

substituting the central k -space by the measurement data of \mathbf{m}^k for $\lambda \rightarrow 0$ and the model prediction $\mathbf{u}_{r,ijk}^k$ for $\lambda \rightarrow \infty$. Since the best metrics scores, that this reconstruction model can achieve, correspond to higher λ value (which is the prediction of DL model), the performance of the recon-

struction model is not considered in the benchmarks with other proposed reconstruction models. The absence of such an intermediate value λ , which yields a better reconstruction result than individual terms, can be explained by the high noise level in the original measurement \mathbf{m}^k .

The $\text{RCAN}_{\mathbb{C}}+\text{E2E}$ model achieved slightly lower median scores for quality metrics, than the $\text{RCAN}_{\mathbb{C}}$ with the same number of training epochs. Moreover, the reference magnitude model $\text{RCAN}_{\mathbb{R}}$ demonstrated better median metric scores for each of metrics.

	$\text{RCAN}_{\mathbb{R}}$	$\text{RCAN}_{\mathbb{C}}$	$\text{RCAN}_{\mathbb{C}}+\text{E2E}$
median SSIM, magnitude, in %	90.35	89.65	89.37
median PSNR, magnitude, in dB	33.69	33.24	33.10
median MSE, magnitude	328	364	376

Table 4.1: Median metrics scores for the fully sampled input. All models are trained with $(120 + 60)$ epochs. Better results for each metric are bold.

This can be particularly explained by the high noise level of the input data, which is explicitly introduced to the output of the reconstruction model in the data-consistency step.

Taking the negligible difference in the metrics scores into account, no single model can be pronounced as the overall best model. Possibly, the data-consistency E2E model can provide better reconstruction quality for the input data, which is lying outside of simulated training data domain (e.g. *in vivo* measurements).

4.5.2 Super-resolution, denoising and undersampling problem

The proposed model can also be applied to the undersampling task, providing reconstructions with high image quality metric scores. However, a decline in these scores was observed as the sampling degree of k -space was reduced, which can be an acceptable trade-off between image quality and measurement duration.

For the same sampling degree, the PF sampling trajectory yielded higher image quality metrics score compared to GS, suggesting its advantage in preserving structural details under limited data conditions. Nevertheless, none of the complex-valued models achieved better performance scores than the magnitude-based DL model, which consistently demonstrated better reconstruction quality across the evaluated sampling schemes.

Sampling degree, in %	median SSIM, magnitude, in %					
	Partial Fourier			Gaussian Sampling		
RCAN _R	RCAN _C	RCAN _C +E2E	RCAN _R	RCAN _C	RCAN _C +E2E	
80	90.06	89.43	89.11	89.76	89.02	87.93
60	89.31	88.58	88.32	88.78	88.06	87.03
55	89.04	88.17	88.01	88.54	87.81	86.81

Sampling degree, in %	median PSNR, magnitude, in dB					
	Partial Fourier			Gaussian Sampling		
RCAN _R	RCAN _C	RCAN _C +E2E	RCAN _R	RCAN _C	RCAN _C +E2E	
80	33.48	33.09	33.05	33.31	32.91	32.56
60	33.04	32.64	32.61	32.79	32.37	32.07
55	32.86	32.47	32.47	32.62	32.22	31.99

Sampling degree, in %	median MSE, magnitude					
	Partial Fourier			Gaussian Sampling		
RCAN _R	RCAN _C	RCAN _C +E2E	RCAN _R	RCAN _C	RCAN _C +E2E	
80	345	377	381	358	393	426
60	382	419	421	404	445	477
55	398	435	435	421	461	486

Table 4.2: Results for the reconstruction of partially sampled input with Partial Fourier and Gaussian Sampling patterns. All models are trained with $(120 + 60)$ epochs. Better results for each metric within the same sampling pattern are bold.

Given the potential bias of the employed performance metrics, coming from their high sensitivity to noise [57] and their limited ability to capture improvements in relevant anatomical structures, experiments with *in vivo* data are essential for draw of relevant conclusions about the performance of the proposed models.

5 Application for *in vivo* data

5.1 Introduction

In previous Chapters 3 and 4 various reconstruction models were introduced, as purely Deep-Learning (DL) models, as well as the DL models embedded with the physical acquisition model. These models were trained and benchmarked on the artificial Ultra-Low-Field (ULF) Magnetic Resonance Imaging (MRI) dataset based on the High-Field (HF) MRI acquisition. All of the proposed reconstruction models, as magnitude-only DL model of Residual Channel Attention Network (RCAN) architecture, complex-valued DL model, and physics-informed DL model demonstrated similar scores in benchmark of image quality metrics, with a small performance gap of magnitude model of less than 1 % for Structural Similarity Index Measure (SSIM) and Peak Signal-to-Noise Ratio (PSNR) metrics and approx. 10 % for Mean-Squared Error (MSE) metric.

However, the insignificant differences in performance among the prepared models do not allow to identify a single best-performing reconstruction model approach. Moreover, since the training dataset is derived from the HF MRI acquisitions of the fastMRI dataset by the known physical acquisition model and purely simulated phase component of the acquisitions, it does not necessarily reflect all the characteristics of real-world ULF MRI acquisitions or may lack of features of a particular ULF MRI scanner. Therefore, in this Chapter, all previously developed models are evaluated and compared on *in vivo* ULF MRI acquisition data.

The *in vivo* data consists of two brain acquisitions obtained with the OSI² ONE [47] scanner [58]. One acquisition was performed with the T_2 weighted contrast, which is the measurement type the models were trained on. In addition, the limits of potential measurement acceleration were tested by undersampling of the k -space by Partial Fourier (PF) and Gaussian Sampling (GS) trajectories, as was introduced in previous Chapter. The second measurement was done with the Proton-Density (PD) contrast and is used to verify whether the reconstruction model for T_2 weighted contrast is applicable for reconstruction of other measurement.

5.2 Methods

The *in vivo* brain imaging experiments were performed at Leiden University Medical Center (LUMC) with the Field Of View (FOV) of $210 \times 200 \times 240 \text{ mm}^3$ and resolution of $5 \times 2 \times 2 \text{ mm}^3$ made with fully sampled three-dimensional Cartesian sampling $42 \times 100 \times 120 \text{ px}^3$ Turbo Spin Echo (TSE) MRI sequence [58]. With the given configuration, measurements of T_2 and PD weighted contrasts were performed.

5.3 Experiments

Reconstruction models prepared in the previous Chapter were constructed to have an input of shape $16 \times 100 \times 120 \text{ px}^3$, while acquired *in vivo* data consists of 42 slices $42 \times 100 \times 120 \text{ px}^3$. Many of the top and bottom slices did not contain brain structures and, therefore, could be safely removed from the input data. For the remaining slices, a continuous sequence of 16 slices (slices 8 to 24 of the original measurement) was selected to approximately match the anatomical structure of the training sub-dataset.

The reconstructions $\bar{\mathbf{u}}$ of the complex-valued *in vivo* acquisitions \mathbf{m}^k were reconstructed with an inverse Fourier transform \mathbf{F}^{-1} and intensities were scaled to have one as maximal value.

$$\bar{\mathbf{u}} = \frac{\mathbf{F}^{-1}\mathbf{m}^k}{\max(|\mathbf{F}^{-1}\mathbf{m}^k|)} \quad (5.1)$$

The reconstruction models RCAN_R, RCAN_C and RCAN_C+E2E, presented in Chapter 4, are considered. The reconstruction with the zero-padded k -space acts as baseline reconstruction reference and denoted as "zero-pad baseline".

Often, for the benchmark of ULF MRI a paired high resolution acquisition with high Signal-to-Noise Ratio (SNR), made with a commercial HF MRI scanner is provided as a reference. For the two ULF MRI measurements no paired reference is provided and models reconstruction quality is only evaluated based on the human visual perception and morphological consistency of the reconstructions.

Alongside with the reconstruction of the fully sampled data, the reconstruction of partially sampled data with PF and GS of 80 %, 60 % and 55 % sampling degrees with the identical sampling trajectories, shown in Figure 7, is performed and compared with the reconstruction results of the fully sampled data.

Reconstruction of the PD weighted acquisition is of particular interest to estimate the applicability of the previously trained model to data from another domain. Reconstruction of the PD weighted acquisition is performed with the same reconstruction models, as T_2 acquisition.

5.4 Results

5.4.1 Brain T2 relaxation time contrast acquisition

Super-resolution and denoising problem

Predictions of the reconstruction models for fully sampled input of shape $16 \times 100 \times 120 \text{ px}^3$ is shown in Figure 27.

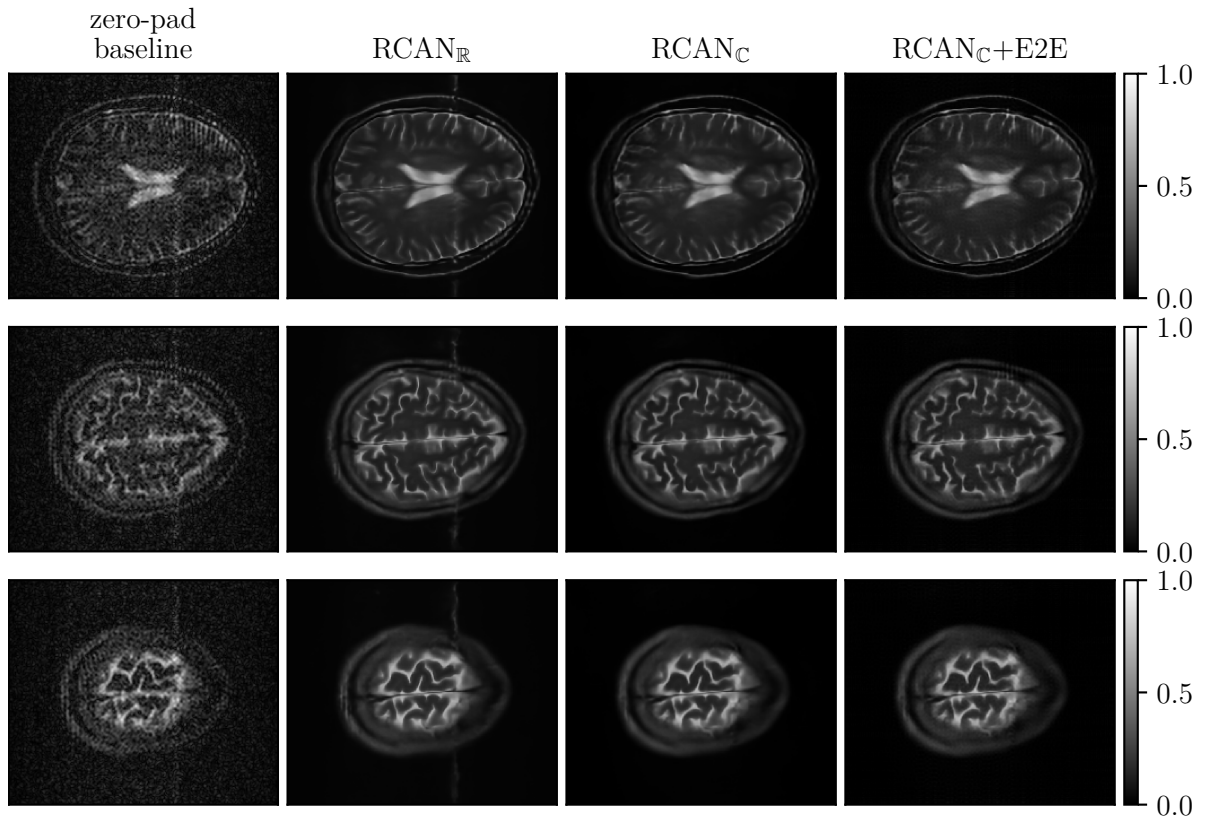


Figure 27: Predictions of reconstruction models for fully sampled T_2 weighted *in vivo* input data. Shown are different slices of the measurements.

Two clearly visible classes of artifacts present in the *in vivo* acquisition. Those are a narrow vertical stripe of higher noise corresponding to the Electromagnetic Interference (EMI) at the specific frequency and a grid of vertical stripes explained by the misalignment of the acquisition parameters, referenced as a "zebra-like" pattern [58].

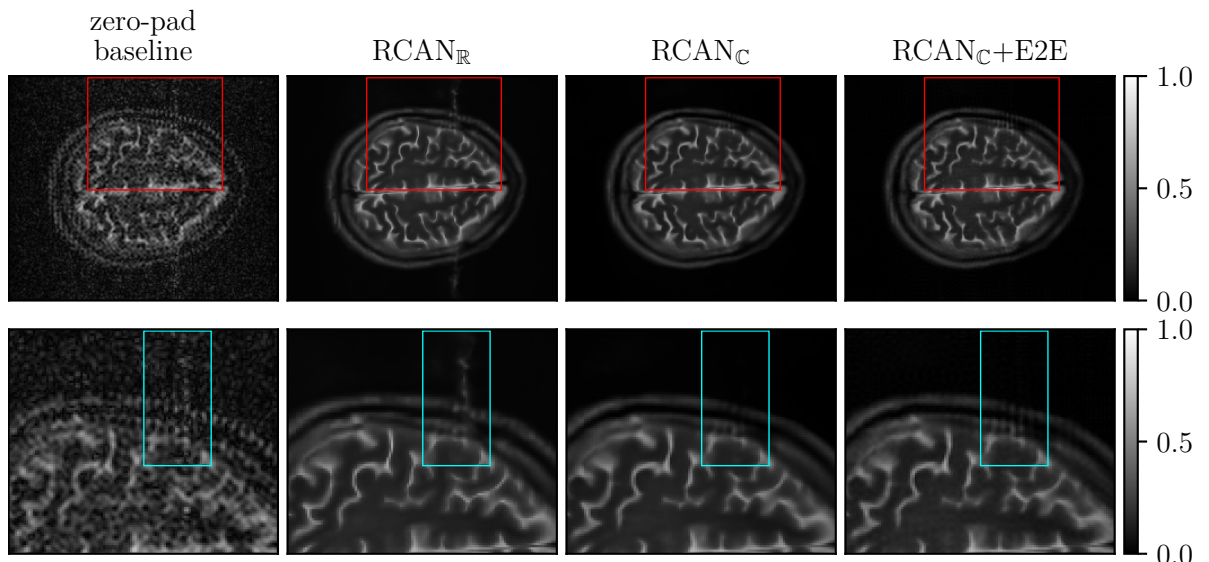


Figure 28: (top) T_2 weighted *in vivo* outputs with (bottom) insets of red rectangles. The region with pronounced EMI caused vertical stripe artifact is marked with aqua rectangle.

All reconstruction models were able to reconstruct the input image with the similar overall quality reducing the noise and increasing the fine structure resolution. While the vertical stripe artifact, highlighted with aqua-coloured rectangle in Figure 28, is present in the zero-pad baseline and $\text{RCAN}_{\mathbb{R}}$ reconstructions, this is missing in $\text{RCAN}_{\mathbb{C}}$ and $\text{RCAN}_{\mathbb{C}}+\text{End-to-End}$ (E2E).

Taking a look into the complex representation of *in vivo* data and predictions of the complex-valued models, shown in Figure 29.

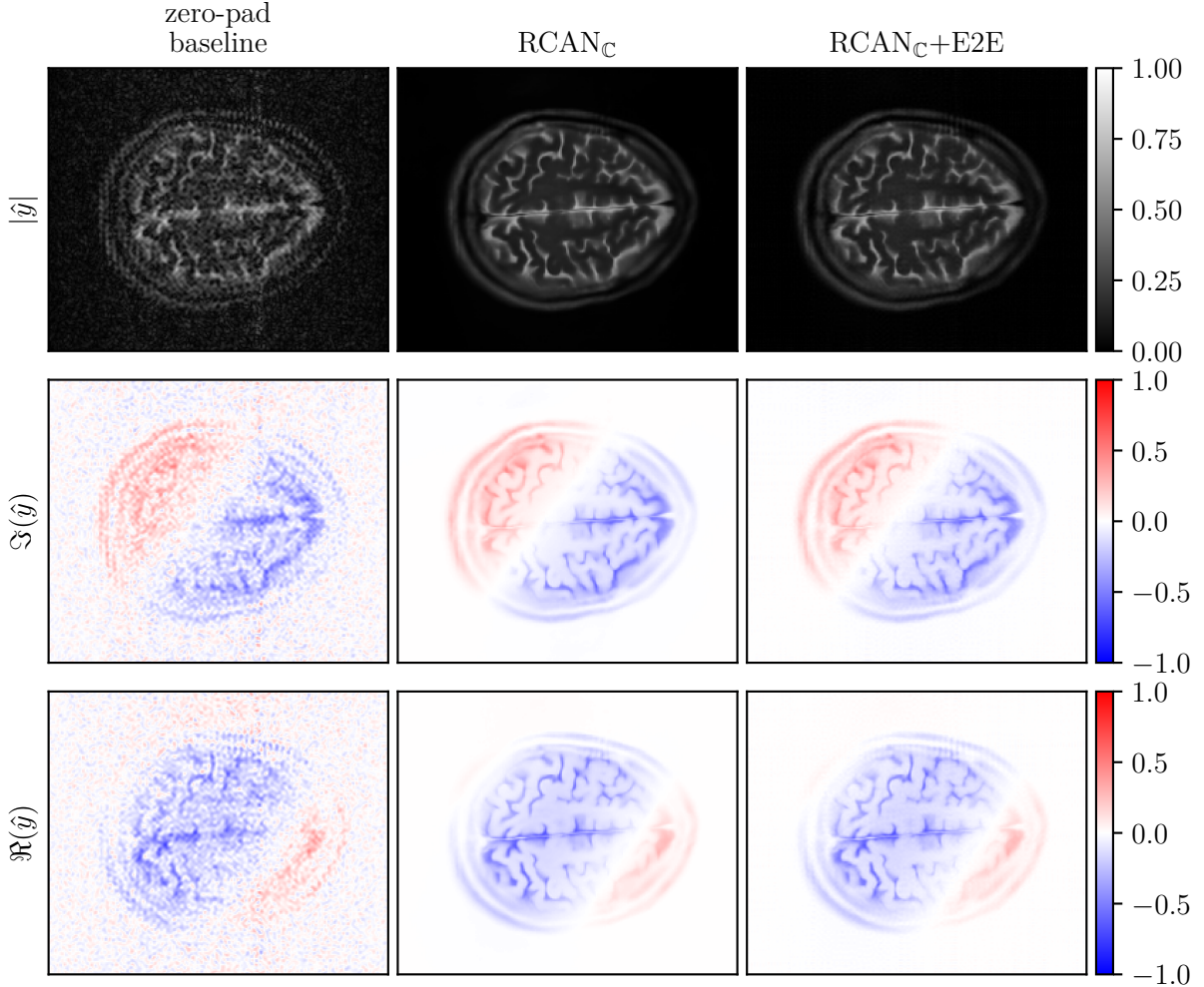


Figure 29: Prediction of complex-valued reconstruction models for T_2 weighted *in vivo* measurement.

While the stripe artifact is clearly visible in the magnitudes domain, this much less deviates from the noise background in the complex-valued domain. An explanation of an absence of such artificial in the outputs of the $\text{RCAN}_{\mathbb{C}}$ based models can be the benefit a complex-valued representation and complex-valued model to dedifferentiate between noise and brain structures. The $\text{RCAN}_{\mathbb{C}}+\text{E2E}$, however, has more pronounced "zebra-like" stripes artifacts on the periphery region of head compared with $\text{RCAN}_{\mathbb{C}}$.

Super-resolution, denoising and undersampling problem

The fully sampled *in vivo* measurement is further artificially undersampled by the PF and GS k -space patterns, in Figures 30 and 31, respectively. The undersampled input data then evaluated

with the reconstruction models trained on the data with matching sampling degree and sampling patterns.

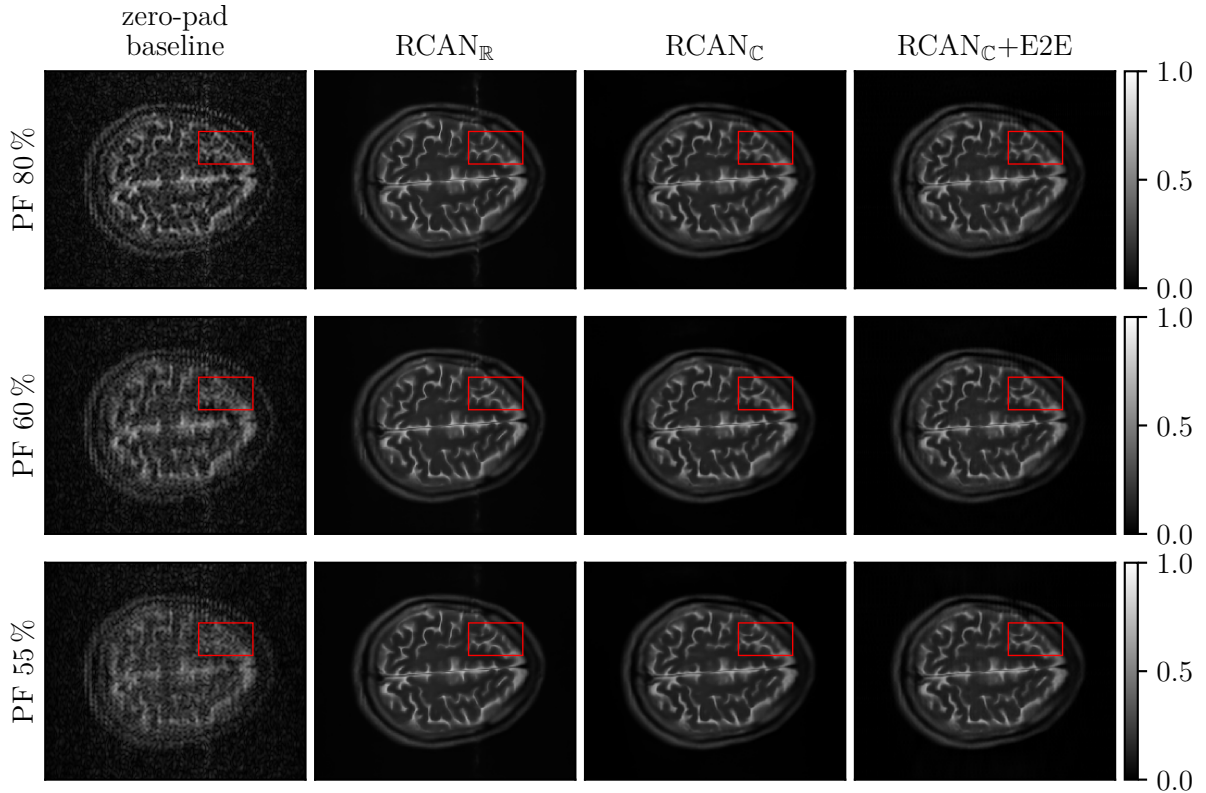


Figure 30: Slices of T_2 weighted *in vivo* acquisition for 80 %, 60 % and 55 % sampling degree with Partial Fourier (PF) pattern. Morphological changes are visible in the region enclosed by red rectangles with decrease of k -space sampling degree.

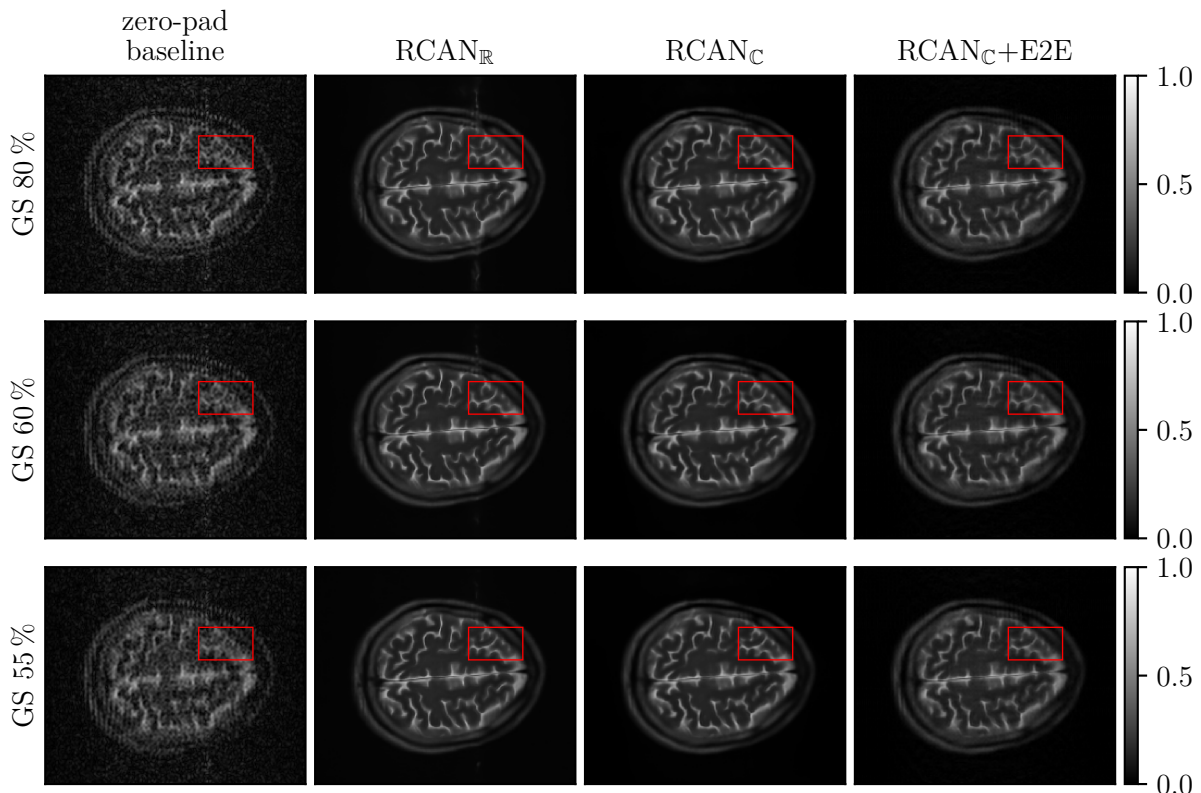


Figure 31: Slices of T_2 weighted *in vivo* acquisition for 80 %, 60 % and 55 % sampling degree with Gaussian Sampling (GS) pattern. Morphological changes are visible in the region enclosed by red rectangles with decrease of k -space sampling degree.

With reduction of sampling degrees for both PF and GS inconsistent changes in morphological structures are visible. The reconstruction models tend to joint the morphological structures.

5.4.2 Brain proton density contrast acquisition

The fully sampled PD weighted acquisitions were evaluated with the $RCAN_R$, $RCAN_C$ and $RCAN_C+E2E$ reconstruction models, which were trained on T_2 weighted contrasts of fully sampled data.

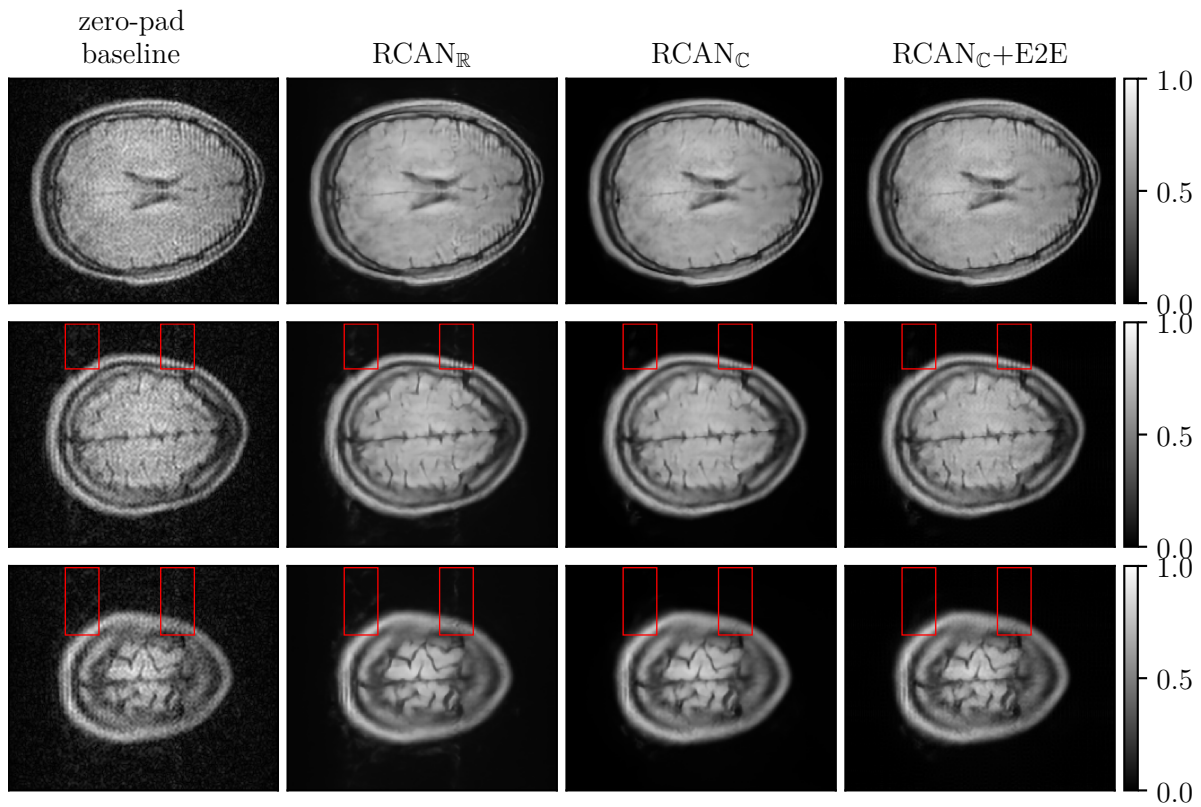


Figure 32: Predictions of reconstruction models for fully sampled PD weighted *in vivo* data. Shown are different slices of the measurements. Regions with vertical stripe noise artifacts are highlighted with red rectangles.

The previously observed behaviour in T_2 weighted measurements shows that complex-valued DL models can more efficiently suppress noise, as demonstrated in the specific case of an artifact in the form of a vertical stripe with a higher noise level.

5.5 Discussion

In this chapter, previously introduced DL models trained with the artificially created ULF MRI dataset, composed from the fastMRI dataset of HF MRI acquisitions, were applied to the reconstruction problem of *in vivo* data, acquired with the prototype of OSI² ONE MRI scanner.

All of the considered models, RCAN_R and RCAN_C, are able to deliver a morphologically consistent reconstruction, successfully solving both super-resolution and denoising problems for the fully sampled T_2 weighted contrast acquisitions.

The *in vivo* measurements exhibited two types of acquisition artifacts. The first was caused by a misalignment of the acquisition settings, resulting in a "zebra-like" vertical stripe pattern. The second originated from the Electromagnetic Interference with a narrow frequency band, yielding a single vertical stripe with a higher noise amplitude. Such distortions of the image were not included in the acquisition model and, therefore, were not present in the train sub-dataset on which the models were trained.

The magnitude-only model RCAN_R is able to reduce the noise and increase the resolution, while the both acquisition artifacts described above were still present in the prediction of the model.

The complex-valued model $\text{RCAN}_{\mathbb{C}}$ is able to not only reduce the noise and increase the resolution of the resulting magnitude, but also provide a consistent complex-valued reconstruction of reduced noise and increased resolution. Moreover, the complex-valued model also eliminated the vertical stripe of higher noise amplitude and mitigated the "zebra-like" vertical stripes pattern, without elimination of the relevant brain structure compared to the magnitude-only model $\text{RCAN}_{\mathbb{R}}$. This feature can be explained by the additional information provided with the real and imaginary components of the data and ability of the DL model to utilise the complex-valued data for better recognition and differentiation of relevant signal and noise.

However, no significant advantages of the use of the physics-informed model $\text{RCAN}_{\mathbb{C}}\text{-E2E}$ in comparison with the $\text{RCAN}_{\mathbb{C}}$ model could have been observed. In contrast, the explicit introduction of data-consistency term made the "zebra-like" stripe pattern artifact more pronounced in the reconstruction result, compared to the prediction of $\text{RCAN}_{\mathbb{C}}$ model alone.

For the reconstruction problem with partially sampled input data, all of the models demonstrated severe morphological distortions with decrease of sampling degree for both of PF and GS sampling trajectories.

In conclusion, the applicability of the models trained on the simulated dataset of T_2 weighted contrast acquisitions, could have been verified for the *in vivo* data of PD weighted contrast, showing the stability of the proposed models in respect to the input data.

6 Conclusion and Outlook

In this thesis, various Deep-Learning (DL) reconstruction models, including one with physics-informed model, were developed and verified for application for noise reduction (*denoising*) and resolution enhancement (*super-resolution*) tasks for acquisitions of Ultra-Low-Field (ULF) Magnetic Resonance Imaging (MRI) scanner. Originally proposed only for the magnitudes, the DL model was adapted to process the complex-valued acquisition data and demonstrated its capability to perform reconstruction not only for the magnitudes images, but for the complex-valued data as well.

In Chapter 3, two complex-valued datasets that emulate ULF acquisitions were derived from the public dataset of High-Field (HF) MRI T_2 weighted contrast brain acquisitions, one reconstructed directly from the acquired multi-coil data using the Coil Sensitivity Map (CSM) retrieval algorithms, and other with the simulated phase information. Despite the fact that the dataset, derived with the estimated CSM, yielded an identical magnitude signal as the dataset of simulated phase information, the first dataset was found unsuitable for further experiments due to the introduction of image artifacts in reconstruction, which are not naturally feasible for an ULF MRI scanner.

Then, based on the dataset of simulated phase information, the complex-valued DL model and magnitudes DL model based on Residual Channel Attention Network (RCAN) architecture, representing a slightly modified version of the model published in [24], were introduced and trained. Both the complex-valued and magnitudes DL models were capable to reduce the noise level and increase the resolution of the low-resolution input image. The proposed models were able to achieve high metrics scores in Structural Similarity Index Measure (SSIM), Peak Signal-to-Noise Ratio (PSNR) and Mean-Squared Error (MSE) image quality metrics across the test sub-dataset and also significantly reduce the width of Q1 and Q3 quantiles in metrics score distributions, compared to the baseline zero-pad reconstruction, achieved by the inverse Fourier transform of the acquired k -space padded with zeros.

So, the proposed reconstruction models increased the SSIM median score from approx. 69 % up to 90 %, the PSNR median score from approx. 29 dB up to 33 dB, and reduced the median MSE by factor of 2.8. The complex-valued DL model was also able to provide denoised and super-resolved data for imaginary and real components, what is not possible with the application of the magnitude-based DL model.

In Chapter 4, the complex-valued DL model was extended with the physical acquisition model and compared with the performance of two models introduced in Chapter 3 for denoising and super-resolution problems. The physics-informed DL model delivered similar results compared to the two DL physics-uninformed models.

Furthermore, the undersampling in k -space was added to the denoising and super-resolution problems. Partial sampling of Partial Fourier (PF) and Gaussian Sampling (GS) k -space sampling patterns with 80 %, 60 % and 55 % sampling degree were considered. For the same degree of sampling, the PF sampling pattern yields better scores for all evaluated image quality metrics.

Finally, in Chapter 5, the previously prepared models were applied on real-world ULF MRI *in*

vivo measurements [58] of T_2 and Proton-Density (PD) weighted contrasts. For the T_2 weighted measurements all proposed DL models, trained on the dataset derived from the HF MRI acquisition, were able to reconstruct the *in vivo* acquisitions. Moreover, the complex-valued based DL models were able to utilise an additional information of the complex-valued input data to mitigate with the Electromagnetic Interference (EMI) artifact present in the *in vivo* data, while the magnitude DL model left the artifact region unaffected. The physics-informed DL model, proposed in the present thesis, could not demonstrate advantage in the reconstruction of the data compared to the complex-valued physics-uninformed DL model.

The proposed reconstruction models were applied to the partially sampled measurement, derived from the fully sampled **in vivo** measurement, indicated significant changes in morphological structures for partially sampled measurements. With reduction of sampling degree, all of the proposed models tend to join the close-lying structures, which were clearly separated from each other in reconstruction of the fully sampled acquisition.

Despite the fact that no advantages of the particular physics-informed deep-learning approach could have been demonstrated in this thesis, the development of a complex-valued dataset and deep-learning model established a framework for further experiments in this regard. With the high-resolution and denoised prediction of the complex-valued data by the deep-learning model, better estimation of B_0 field inhomogeneities can possibly be performed, which is crucial for the ULF MRI system [28]. Alternative sampling patterns as high time-efficient spiral- or radiant-like k -space sampling trajectories, as well as alternative architectures for deep-learning models can be considered, such as, for example, Denoising Diffusion Probabilistic Models (DDPMs) [59, 60], which are widely used for the inverse problems [61] and particularly for MRI reconstruction problem [62]. Moreover, other physics-informed reconstruction algorithms, which have already demonstrated better reconstruction results for DDPMs [63–65], can be challenged for the reconstruction problem of ULF MRI.

Bibliography

- [1] “MRI scans Germany 2022,” Statista. (Sep. 2024), [Online]. Available: <https://www.statista.com/statistics/863499/magnetic-resonance-imaging-scan-examinations-in-germany/?srsltid=AfmB0or1Ib4AIHtsirdDFiiZ0RVoqjS0SWXub3VF9N-D5aMaubgTotce> (visited on Sep. 22, 2025).
- [2] F. Bloch *et al.*, “The Nuclear Induction Experiment,” *Physical Review*, vol. 70, no. 7–8, pp. 474–485, Oct. 1, 1946, ISSN: 0031-899X. DOI: 10.1103/physrev.70.474. [Online]. Available: <https://link.aps.org/doi/10.1103/PhysRev.70.474> (visited on Jul. 24, 2025).
- [3] P. C. Lauterbur, “Image Formation by Induced Local Interactions: Examples Employing Nuclear Magnetic Resonance,” *Nature*, vol. 242, no. 5394, pp. 190–191, Mar. 1973, ISSN: 0028-0836, 1476-4687. DOI: 10.1038/242190a0. [Online]. Available: <https://www.nature.com/articles/242190a0> (visited on Jul. 24, 2025).
- [4] P. Mansfield, “Multi-planar image formation using NMR spin echoes,” *Journal of Physics C: Solid State Physics*, vol. 10, no. 3, pp. L55–L58, Feb. 14, 1977, ISSN: 0022-3719. DOI: 10.1088/0022-3719/10/3/004. [Online]. Available: <https://iopscience.iop.org/article/10.1088/0022-3719/10/3/004> (visited on Jul. 24, 2025).
- [5] “The Nobel Prize in Physiology or Medicine 2003,” NobelPrize.org. (Oct. 6, 2003), [Online]. Available: <https://www.nobelprize.org/prizes/medicine/2003/summary/> (visited on Jul. 24, 2025).
- [6] L. Winter *et al.*, “Open Source Medical Devices for Innovation, Education and Global Health: Case Study of Open Source Magnetic Resonance Imaging,” in *Co-Creation*, T. Redlich *et al.*, Eds., Cham: Springer International Publishing, 2019, pp. 147–163, ISBN: 978-3-319-97787-4. DOI: 10.1007/978-3-319-97788-1_12. [Online]. Available: https://link.springer.com/10.1007/978-3-319-97788-1_12 (visited on Sep. 25, 2025).
- [7] “Magnetic resonance imaging (MRI) units,” OECD. (Aug. 21, 2025), [Online]. Available: <https://www.oecd.org/en/data/indicators/magnetic-resonance-imaging-mri-units.html> (visited on Sep. 22, 2025).
- [8] M. Sarracanie *et al.*, “Low-Cost High-Performance MRI,” *Scientific Reports*, vol. 5, no. 1, Oct. 15, 2015, ISSN: 2045-2322. DOI: 10.1038/srep15177. [Online]. Available: <https://www.nature.com/articles/srep15177> (visited on Jul. 24, 2025).
- [9] C. Z. Cooley *et al.*, “A portable scanner for magnetic resonance imaging of the brain,” *Nature Biomedical Engineering*, vol. 5, no. 3, pp. 229–239, Nov. 23, 2020, ISSN: 2157-846X. DOI: 10.1038/s41551-020-00641-5. [Online]. Available: <https://www.nature.com/articles/s41551-020-00641-5> (visited on Jul. 24, 2025).
- [10] Y. Liu *et al.*, “A low-cost and shielding-free ultra-low-field brain MRI scanner,” *Nature Communications*, vol. 12, no. 1, p. 7238, Dec. 14, 2021, ISSN: 2041-1723. DOI: 10.1038/s41467-021-27317-1. [Online]. Available: <https://www.nature.com/articles/s41467-021-27317-1> (visited on Oct. 22, 2024).

[11] S. C. L. Deoni *et al.*, “Development of a mobile low-field MRI scanner,” *Scientific Reports*, vol. 12, no. 1, Apr. 5, 2022, ISSN: 2045-2322. DOI: 10.1038/s41598-022-09760-2. [Online]. Available: <https://www.nature.com/articles/s41598-022-09760-2> (visited on Jul. 24, 2025).

[12] L. Winter. “First open-source MRI scanner presented: The OSI² ONE – Open Source Imaging.” (Jan. 9, 2023), [Online]. Available: <https://www.opensourceimaging.org/2023/01/09/first-open-source-mri-scanner-presented-the-osii-one/> (visited on Jun. 11, 2025).

[13] J. Vosshenrich *et al.*, “Ökonomische Aspekte der Niederfeld-Magnetresonanztomographie,” *Der Radiologe*, vol. 62, no. 5, pp. 400–404, May 1, 2022, ISSN: 1432-2102. DOI: 10.1007/s00117-022-00986-9. [Online]. Available: <https://doi.org/10.1007/s00117-022-00986-9> (visited on Sep. 22, 2025).

[14] S. Murali *et al.*, “Bringing MRI to low- and middle-income countries: Directions, challenges and potential solutions,” *NMR in Biomedicine*, vol. 37, no. 7, e4992, Jul. 2024, ISSN: 0952-3480, 1099-1492. DOI: 10.1002/nbm.4992. [Online]. Available: <https://analyticalscienc ejournals.onlinelibrary.wiley.com/doi/10.1002/nbm.4992> (visited on Sep. 22, 2025).

[15] “The Nobel Prize in Physics 2024,” NobelPrize.org. (Oct. 8, 2024), [Online]. Available: <https://www.nobelprize.org/prizes/physics/2024/summary/> (visited on Sep. 24, 2025).

[16] K. Zhang *et al.*, “Beyond a Gaussian Denoiser: Residual Learning of Deep CNN for Image Denoising,” *IEEE Transactions on Image Processing*, vol. 26, no. 7, pp. 3142–3155, Jul. 2017, ISSN: 1057-7149, 1941-0042. DOI: 10.1109/tip.2017.2662206. [Online]. Available: <https://ieeexplore.ieee.org/document/7839189/> (visited on Jul. 25, 2025).

[17] C. Dong *et al.*, “Image Super-Resolution Using Deep Convolutional Networks,” *IEEE Transactions on Pattern Analysis and Machine Intelligence*, vol. 38, no. 2, pp. 295–307, Feb. 1, 2016, ISSN: 0162-8828, 2160-9292. DOI: 10.1109/tpami.2015.2439281. [Online]. Available: <https://ieeexplore.ieee.org/document/7115171/> (visited on Jul. 25, 2025).

[18] R. Kushol *et al.*, “Effects of MRI scanner manufacturers in classification tasks with deep learning models,” *Scientific Reports*, vol. 13, no. 1, p. 16791, Oct. 5, 2023, ISSN: 2045-2322. DOI: 10.1038/s41598-023-43715-5. [Online]. Available: <https://www.nature.com/articles/s41598-023-43715-5> (visited on Sep. 24, 2025).

[19] M. Raissi *et al.*, “Physics-informed neural networks: A deep learning framework for solving forward and inverse problems involving nonlinear partial differential equations,” *Journal of Computational Physics*, vol. 378, pp. 686–707, Feb. 2019, ISSN: 00219991. DOI: 10.1016/j.jcp.2018.10.045. [Online]. Available: <https://linkinghub.elsevier.com/retrieve/pii/S0021999118307125> (visited on Sep. 22, 2025).

[20] C. Qian *et al.* “Physics-informed Deep Diffusion MRI Reconstruction with Synthetic Data: Break Training Data Bottleneck in Artificial Intelligence.” version 6. (2022), [Online]. Available: <https://arxiv.org/abs/2210.11388> (visited on Sep. 24, 2025), pre-published.

[21] F. F. Zimmermann *et al.*, “PINQI: An End-to-End Physics-Informed Approach to Learned Quantitative MRI Reconstruction,” *IEEE Transactions on Computational Imaging*, vol. 10, pp. 628–639, 2024, ISSN: 2333-9403, 2334-0118, 2573-0436. DOI: 10.1109/TCI.2024.3388869. [Online]. Available: <https://ieeexplore.ieee.org/document/10499888/> (visited on Sep. 22, 2025).

[22] M. L. De Leeuw Den Bouter *et al.*, “Deep learning-based single image super-resolution for low-field MR brain images,” *Scientific Reports*, vol. 12, no. 1, p. 6362, Apr. 16, 2022, ISSN: 2045-2322. DOI: 10.1038/s41598-022-10298-6. [Online]. Available: <https://www.nature.com/articles/s41598-022-10298-6> (visited on Oct. 24, 2024).

[23] V. Lau *et al.*, “Pushing the limits of low-cost ultra-low-field MRI by dual-acquisition deep learning 3D superresolution,” *Magnetic Resonance in Medicine*, vol. 90, no. 2, pp. 400–416, Aug. 2023, ISSN: 1522-2594. DOI: 10.1002/mrm.29642. PMID: 37010491.

[24] C. Man *et al.*, “Deep learning enabled fast 3D brain MRI at 0.055 tesla,” *Science Advances*, vol. 9, no. 38, eadi9327, Sep. 22, 2023. DOI: 10.1126/sciadv.ad19327. [Online]. Available: <https://www.science.org/doi/10.1126/sciadv.ad19327> (visited on May 14, 2025).

[25] R. Ayde *et al.*, “MRI at low field: A review of software solutions for improving SNR,” *NMR in Biomedicine*, e5268, Oct. 7, 2024, ISSN: 0952-3480, 1099-1492. DOI: 10.1002/nbm.5268. [Online]. Available: <https://analyticalsciencejournals.onlinelibrary.wiley.com/doi/10.1002/nbm.5268> (visited on Oct. 15, 2024).

[26] A. Salehi *et al.*, “Denoising low-field MR images with a deep learning algorithm based on simulated data from easily accessible open-source software,” *Journal of Magnetic Resonance*, vol. 370, p. 107812, Jan. 2025, ISSN: 10907807. DOI: 10.1016/j.jmr.2024.107812. [Online]. Available: <https://linkinghub.elsevier.com/retrieve/pii/S1090780724001964> (visited on Sep. 24, 2025).

[27] “Hyperfine Receives FDA Clearance for Deep Learning Portable MRI, Defining the Future of Life-Saving Diagnostics | Hyperfine, Inc.” (Nov. 29, 2021), [Online]. Available: <https://investors.hyperfine.io/news-releases/news-release-details/hyperfine-receives-fda-clearance-deep-learning-portable-mri/> (visited on Sep. 24, 2025).

[28] D. Schote *et al.*, “Joint B_0 and Image Reconstruction in Low-Field MRI by Physics-Informed Deep-Learning,” *IEEE Transactions on Biomedical Engineering*, vol. 71, no. 10, pp. 2842–2853, Oct. 2024, ISSN: 0018-9294, 1558-2531. DOI: 10.1109/TBME.2024.3396223. [Online]. Available: <https://ieeexplore.ieee.org/document/10517636/> (visited on Oct. 15, 2024).

[29] R. W. Brown *et al.*, *Magnetic Resonance Imaging: Physical Principles and Sequence Design*, Second edition. Hoboken, New Jersey: John Wiley & Sons, Inc, 2014, 944 pp., ISBN: 978-0-471-72085-0.

[30] D. W. McRobbie *et al.*, *MRI from Picture to Proton*, Third edition. Cambridge ; New York: University Printing House, Cambridge University Press, 2017, 382 pp., ISBN: 978-1-107-64323-9.

[31] M. A. Bernstein *et al.*, *Handbook of MRI Pulse Sequences*. Amsterdam ; Boston: Academic Press, 2004, 1017 pp., ISBN: 978-0-12-092861-3.

[32] D. B. Plewes *et al.*, “Physics of MRI: A primer,” *Journal of Magnetic Resonance Imaging*, vol. 35, no. 5, pp. 1038–1054, May 2012, ISSN: 1053-1807, 1522-2586. DOI: 10.1002/jmri.23642. [Online]. Available: <https://onlinelibrary.wiley.com/doi/10.1002/jmri.23642> (visited on Oct. 15, 2024).

[33] H. Gudbjartsson *et al.*, “The rician distribution of noisy mri data,” *Magnetic Resonance in Medicine*, vol. 34, no. 6, pp. 910–914, Dec. 1995, ISSN: 0740-3194, 1522-2594. DOI: 10.1002/mrm.1910340618. [Online]. Available: <https://onlinelibrary.wiley.com/doi/10.1002/mrm.1910340618> (visited on Oct. 19, 2025).

[34] S. Inati *et al.*, “A solution to the phase problem in adaptive coil combination,” presented at the The 21st Annual Meeting of ISMRM, Salt Lake City, USA, 2013.

[35] D. O. Walsh *et al.*, “Adaptive reconstruction of phased array MR imagery,” *Magnetic Resonance in Medicine*, vol. 43, no. 5, pp. 682–690, May 2000, ISSN: 0740-3194, 1522-2594. DOI: 10.1002/(SICI)1522-2594(200005)43:5<682::AID-MRM10>3.0.CO;2-G. [Online]. Available: [https://onlinelibrary.wiley.com/doi/10.1002/\(SICI\)1522-2594\(200005\)43:5%3C682::AID-MRM10%3E3.0.CO;2-G](https://onlinelibrary.wiley.com/doi/10.1002/(SICI)1522-2594(200005)43:5%3C682::AID-MRM10%3E3.0.CO;2-G) (visited on Nov. 6, 2024).

[36] M. Uecker *et al.*, “ESPIRiT—an eigenvalue approach to autocalibrating parallel MRI: Where SENSE meets GRAPPA,” *Magnetic Resonance in Medicine*, vol. 71, no. 3, pp. 990–1001, Mar. 2014, ISSN: 0740-3194, 1522-2594. DOI: 10.1002/mrm.24751. [Online]. Available: <https://onlinelibrary.wiley.com/doi/10.1002/mrm.24751> (visited on Oct. 29, 2024).

[37] L. I. Rudin *et al.*, “Nonlinear total variation based noise removal algorithms,” *Physica D: Nonlinear Phenomena*, vol. 60, no. 1–4, pp. 259–268, Nov. 1992, ISSN: 01672789. DOI: 10.1016/0167-2789(92)90242-F. [Online]. Available: <https://linkinghub.elsevier.com/retrieve/pii/016727899290242F> (visited on Oct. 19, 2025).

[38] K. T. Block *et al.*, “Undersampled radial MRI with multiple coils. Iterative image reconstruction using a total variation constraint,” *Magnetic Resonance in Medicine*, vol. 57, no. 6, pp. 1086–1098, Jun. 2007, ISSN: 0740-3194, 1522-2594. DOI: 10.1002/mrm.21236. [Online]. Available: <https://onlinelibrary.wiley.com/doi/10.1002/mrm.21236> (visited on Oct. 19, 2025).

[39] M. Lustig *et al.*, “Sparse MRI: The application of compressed sensing for rapid MR imaging,” *Magnetic Resonance in Medicine*, vol. 58, no. 6, pp. 1182–1195, 2007, ISSN: 1522-2594. DOI: 10.1002/mrm.21391. [Online]. Available: <https://onlinelibrary.wiley.com/doi/abs/10.1002/mrm.21391> (visited on May 21, 2025).

[40] L. Zhang *et al.*, “Image Restoration: From Sparse and Low-Rank Priors to Deep Priors [Lecture Notes],” *IEEE Signal Processing Magazine*, vol. 34, no. 5, pp. 172–179, Sep. 2017, ISSN: 1053-5888. DOI: 10.1109/MSP.2017.2717489. [Online]. Available: <http://ieeexplore.ieee.org/document/8026108/> (visited on Oct. 19, 2025).

[41] K. Zhang *et al.*, “Learning Deep CNN Denoiser Prior for Image Restoration,” in *2017 IEEE Conference on Computer Vision and Pattern Recognition (CVPR)*, Honolulu, HI: IEEE, Jul. 2017, pp. 2808–2817, ISBN: 978-1-5386-0457-1. DOI: 10.1109/CVPR.2017.300. [Online]. Available: <http://ieeexplore.ieee.org/document/8099783/> (visited on Oct. 19, 2025).

[42] J. R. Chang *et al.*, “One Network to Solve Them All — Solving Linear Inverse Problems Using Deep Projection Models,” in *2017 IEEE International Conference on Computer Vision (ICCV)*, Venice: IEEE, Oct. 2017, pp. 5889–5898, ISBN: 978-1-5386-1032-9. DOI: 10.1109/ICCV.2017.627. [Online]. Available: <https://ieeexplore.ieee.org/document/8237889/> (visited on Oct. 19, 2025).

[43] K. H. Jin *et al.*, “Deep Convolutional Neural Network for Inverse Problems in Imaging,” *IEEE Transactions on Image Processing*, vol. 26, no. 9, pp. 4509–4522, Sep. 2017, ISSN: 1057-7149, 1941-0042. DOI: 10.1109/TIP.2017.2713099. [Online]. Available: <http://ieeexplore.ieee.org/document/7949028/> (visited on Oct. 5, 2025).

[44] Y. Zhang *et al.*, “Image Super-Resolution Using Very Deep Residual Channel Attention Networks,” in *Computer Vision – ECCV 2018*, V. Ferrari *et al.*, Eds., vol. 11211, Cham: Springer International Publishing, 2018, pp. 294–310, ISBN: 978-3-030-01233-5. DOI: 10.1007/978-3-030-01234-2_18. [Online]. Available: https://link.springer.com/10.1007/978-3-030-01234-2_18 (visited on Sep. 9, 2025).

[45] E. Cole *et al.*, “Analysis of deep complex-valued convolutional neural networks for MRI reconstruction and phase-focused applications,” *Magnetic Resonance in Medicine*, vol. 86, no. 2, pp. 1093–1109, Aug. 2021, ISSN: 0740-3194, 1522-2594. DOI: 10.1002/mrm.28733. [Online]. Available: <https://onlinelibrary.wiley.com/doi/10.1002/mrm.28733> (visited on Jul. 1, 2025).

[46] M. Ganeshkumar *et al.*, “Fat–water MRI separation using deep complex convolution network,” *Magnetic Resonance Materials in Physics, Biology and Medicine*, Jul. 3, 2025, ISSN: 1352-8661. DOI: 10.1007/s10334-025-01268-w. [Online]. Available: <https://link.springer.com/10.1007/s10334-025-01268-w> (visited on Sep. 25, 2025).

[47] “OSI² ONE MR Scanner – Open Source Imaging.” (2022), [Online]. Available: <https://www.opensourceimaging.org/project/osii-one/> (visited on Sep. 29, 2025).

[48] K. T. Islam *et al.*, “Improving portable low-field MRI image quality through image-to-image translation using paired low- and high-field images,” *Scientific Reports*, vol. 13, no. 1, p. 21183, Dec. 1, 2023, ISSN: 2045-2322. DOI: 10.1038/s41598-023-48438-1. [Online]. Available: <https://www.nature.com/articles/s41598-023-48438-1> (visited on Sep. 25, 2025).

[49] J. Zbontar *et al.* “fastMRI: An Open Dataset and Benchmarks for Accelerated MRI.” arXiv: 1811.08839 [cs]. (Dec. 11, 2019), [Online]. Available: <http://arxiv.org/abs/1811.08839> (visited on Jun. 11, 2025), pre-published.

[50] A. Paszke *et al.* “PyTorch: An Imperative Style, High-Performance Deep Learning Library.” arXiv: 1912.01703 [cs]. (Dec. 3, 2019), [Online]. Available: <http://arxiv.org/abs/1912.01703> (visited on Oct. 21, 2025), pre-published.

[51] F. F. Zimmermann *et al.*, *MRpro - PyTorch-based MR image reconstruction and processing package*, version v0.250513, Zenodo, May 13, 2025. DOI: 10.5281/zenodo.15396025. [Online]. Available: <https://zenodo.org/records/15396025> (visited on May 14, 2025).

[52] V. Antun *et al.*, “On instabilities of deep learning in image reconstruction and the potential costs of AI,” *Proceedings of the National Academy of Sciences*, vol. 117, no. 48, pp. 30 088–30 095, Dec. 2020, ISSN: 0027-8424, 1091-6490. DOI: 10.1073/pnas.1907377117. [Online]. Available: <https://pnas.org/doi/full/10.1073/pnas.1907377117> (visited on Oct. 10, 2025).

[53] J. Schlemper *et al.*, “A Deep Cascade of Convolutional Neural Networks for Dynamic MR Image Reconstruction,” *IEEE Transactions on Medical Imaging*, vol. 37, no. 2, pp. 491–503, Feb. 2018, ISSN: 0278-0062, 1558-254X. DOI: 10.1109/TMI.2017.2760978. [Online]. Available: <https://ieeexplore.ieee.org/document/8067520/> (visited on Oct. 19, 2025).

[54] H. K. Aggarwal *et al.*, “MoDL: Model-Based Deep Learning Architecture for Inverse Problems,” *IEEE Transactions on Medical Imaging*, vol. 38, no. 2, pp. 394–405, Feb. 2019, ISSN: 0278-0062, 1558-254X. DOI: 10.1109/tmi.2018.2865356. [Online]. Available: <https://ieeexplore.ieee.org/document/8434321/> (visited on Jul. 23, 2025).

[55] H. K. Aggarwal *et al.*, “J-MoDL: Joint Model-Based Deep Learning for Optimized Sampling and Reconstruction,” *IEEE Journal of Selected Topics in Signal Processing*, vol. 14, no. 6, pp. 1151–1162, Oct. 2020, ISSN: 1932-4553, 1941-0484. DOI: 10.1109/JSTSP.2020.3004094. [Online]. Available: <https://ieeexplore.ieee.org/document/9122388/> (visited on Oct. 10, 2025).

[56] K. Lin *et al.*, “Robustness of deep learning for accelerated MRI: Benefits of diverse training data,” *Proceedings of Machine Learning Research*, vol. 235, pp. 30 018–30 041, 2024, ISSN: 2640-3498.

[57] M. Dohmen *et al.*, “Similarity and quality metrics for MR image-to-image translation,” *Scientific Reports*, vol. 15, no. 1, p. 3853, Jan. 31, 2025, ISSN: 2045-2322. DOI: 10.1038/s41598-025-87358-0. [Online]. Available: <https://www.nature.com/articles/s41598-025-87358-0> (visited on Sep. 16, 2025).

[58] D. Schote *et al.*, “Nexus: A versatile console for advanced low-field MRI,” *Magnetic Resonance in Medicine*, vol. 93, no. 5, pp. 2224–2238, May 2025, ISSN: 0740-3194, 1522-2594. DOI: 10.1002/mrm.30406. [Online]. Available: <https://onlinelibrary.wiley.com/doi/10.1002/mrm.30406> (visited on Sep. 29, 2025).

[59] J. Ho *et al.* “Denoising Diffusion Probabilistic Models.” version 2. (2020), [Online]. Available: <https://arxiv.org/abs/2006.11239> (visited on Sep. 1, 2025), pre-published.

[60] Y. Song *et al.*, “Score-Based Generative Modeling through Stochastic Differential Equations,” presented at the International Conference on Learning Representations, Oct. 2, 2020. [Online]. Available: <https://openreview.net/forum?id=PxTIG12RRHS> (visited on Sep. 12, 2025).

[61] G. Daras *et al.* “A Survey on Diffusion Models for Inverse Problems.” arXiv: 2410.00083 [cs]. (Sep. 30, 2024), [Online]. Available: <http://arxiv.org/abs/2410.00083> (visited on Sep. 1, 2025), pre-published.

[62] W. Wang *et al.*, “Diffusion model for medical image denoising, reconstruction and translation,” *Computerized Medical Imaging and Graphics*, vol. 124, p. 102593, Sep. 2025, ISSN: 08956111. DOI: 10.1016/j.compmedimag.2025.102593. [Online]. Available: <https://linkinghub.elsevier.com/retrieve/pii/S0895611125001028> (visited on Oct. 19, 2025).

[63] H. Chung *et al.* “MR Image Denoising and Super-Resolution Using Regularized Reverse Diffusion.” version 1. (2022), [Online]. Available: <https://arxiv.org/abs/2203.12621> (visited on Sep. 7, 2025), pre-published.

[64] H. Chung *et al.* “Diffusion Posterior Sampling for General Noisy Inverse Problems.” arXiv: 2209.14687 [stat]. (May 20, 2024), [Online]. Available: <http://arxiv.org/abs/2209.14687> (visited on Sep. 1, 2025), pre-published.

[65] X. Meng *et al.*, “Diffusion Model Based Posterior Sampling for Noisy Linear Inverse Problems,” presented at the The 16th Asian Conference on Machine Learning (Conference Track), Oct. 16, 2024. [Online]. Available: <https://openreview.net/forum?id=A07d0PMRqc> (visited on Sep. 12, 2025).

Acknowledgment

It would not have been possible for me to achieve the results presented in this thesis without the help and support of others.

I would like to express my sincere thanks to the following people. The greatest thanks are due to Dr. Christoph Kolbitsch for the opportunity to write my Master thesis in his working group, and to my supervisor, David Schote, without whose knowledge and expertise in the research field the presented work would not have been possible.

I would also like to express my gratitude to Felix Zimmermann and Dr. Andreas Kofler, who provided enormous help in clarifying the material, sharing their experience and expertise, and thanks Kimon Hadjikiriakos for emotional support during my work.